frontiers in Marine Science

TYPE Original Research
PUBLISHED 12 March 2026
DOI 10.3389/fmars.2026.1750403

OPEN ACCESS

EDITED BY
Wu Men,
Nanjing University of Information Science and Technology, China

REVIEWED BY
Peng Zhou,
Ministry of Natural Resources of the People's Republic of China, China
Hao Ma,
Tsinghua University, China

*CORRESPONDENCE
Massimiliano Iurcev
miurcev@ogs.it

RECEIVED 20 November 2025
REVISED 28 January 2026
ACCEPTED 04 February 2026
PUBLISHED 12 March 2026

CITATION
Salmassian B, Iurcev M, Trebbi A and Coren F (2026) Identification and characterization of gamma radiation anomalies along the Trieste–Panarea routes aboard R/V Laura Bassi. *Front. Mar. Sci.* 13:1750403. doi: 10.3389/fmars.2026.1750403

Identification and characterization of gamma radiation anomalies along the Trieste–Panarea routes aboard R/V Laura Bassi

Behzad Salmassian, Massimiliano Iurcev*, Alessio Trebbi and Franco Coren

National Institute of Oceanography and Applied Geophysics (OGS), Centre for Management of Maritime Infrastructure (CGN), Sgonico, Trieste, Italy

Objective: This study aimed to identify, characterize, and determine the origin of semi-persistent gamma radiation anomalies in the Adriatic Sea along the Trieste-Panarea transect, establishing a high resolution radiometric baseline and assessing the influence of environmental parameters.
Methods: *In situ* gamma-ray spectrometry was conducted using an RS-250 NaI (Tl) detector aboard the R/V Laura Bassi during four research cruises, covering a total distance of over 2500 nautical miles. The spectrometer was configured with 1024 energy channels with range 3 keV and provided a resolution of 6-7% at the 662 keV photopeak of ^{137}Cs. More than 4000 recordings of the total gamma-ray count rate and full-spectrum data were collected. These radiological data were precisely synchronized and correlated with contemporaneous bathymetric, wind speed, air temperature, and humidity data.
Results: Three persistent anomaly regions were identified in the Central Adriatic, Southern Adriatic, and Strait of Otranto, with peak total counts per 10-minute sample of 34,659, 76,854, and 32,415, respectively. Spectral analysis revealed these are primarily sourced from natural Uranium (^{214}Bi, ^{214}Pb), Potassium (^{40}K), and Thorium (^{208}Tl, ^{212}Bi) decay series radionuclides, with a negligible anthropogenic ^{137}Cs contribution. Correlation analyses showed weak relationships with environmental variables ($R^2 < 0.25$ for wind, temperature, humidity, depth), confirming the anomalies are not artifacts of atmospheric or surface conditions but are linked to seabed processes.
Conclusion: The identified anomalies are natural features resulting from the oceanographic focusing of clay-rich, radiogenic sediments in specific depositional zones. This work provides a validated methodological inspection framework and a critical baseline for future geophysical mapping, environmental monitoring, and radiological assessment in the research cruises.

KEYWORDS
Adriatic Sea, Aeolian Islands, anthropogenic radionuclides, marine gamma-ray spectrometry, natural radionuclides, radiation anomaly, environmental radiation

1 Introduction

The Marine Gamma-ray Spectrometry (MGRS) provides an effective method to directly decode the hidden geochemical tapestry of the seafloor, providing detailed information into its formation and composition (Jones, 2001). Its fundamental principle lies in detecting the gamma-ray emissions from radionuclide elements, providing a non-invasive proxy for the mineralogical and chemical composition of the submerged substrate ((IAEA), I.A.E.A., IAEA-TECDOC-1363, 2003). This is particularly valuable in marine environments, where continuous, high resolution spatial data can be acquired efficiently over large areas that are otherwise difficult to sample directly (Tyler, 1994). From a geological perspective, MGRS data are indispensable for sediment provenance studies and mapping lithological variations (Wilford and Minty, 2006). Elevated concentrations of Thorium and Potassium, for instance, are strongly correlated with clay rich deposits and Potassium bearing minerals like feldspar, helping to distinguish these from quartzes sands or carbonates (Dickson and Scott, 1997). Geophysicists integrate these radiometric patterns with other datasets like seismic reflection profiles and bathymetry to reconstruct paleo depositional environments and sediment transport pathways. A premier application of MGRS is the identification of hydrothermal alteration zones associated with seafloor vent systems. Circulating hydrothermal fluids can selectively leach, transport, and re precipitate radionuclides, particularly Uranium and Radium decay series, creating sharp and detectable anomalies at the sediment water interface. These anomalies act as a direct indicator of subsurface fluid flow processes and mineralization (Beamish and Farr, 2013). Furthermore, MGRS contributes significantly to structural geology and resource exploration. Fault systems and fracture zones, which can act as conduits for fluid flow, often present as linear radiometric features. Similarly, placer deposits containing heavy minerals like monazite (enriched in Th) or zircon (enriched in U) can be located through their distinct spectral signatures (Dickson and Scott, 1997). By providing a unique window into the geochemical properties of the seafloor, MGRS is an essential component of integrated marine geological mapping and a powerful method for understanding fluid rock interactions at a fundamental level.

On the other hand, MGRS serves as a critical monitoring tool for detecting and mapping the distribution of anthropogenic radionuclides in seafloor sediments and the water column (Aarkrog, 2003). Its fundamental principle lies in identifying the distinct gamma-ray emissions from human made isotopes, providing a non invasive method to trace contamination events and assess their environmental persistence ((IAEA), I.A.E.A., IAEA-TECDOC-1363, 2003). This is particularly valuable in marine environments, where it allows for the rapid screening and spatial delineation of contamination over large areas that are difficult to sample conventionally (Tyler, 1994). From an environmental perspective, MGRS data are indispensable for identifying the source term and dispersal pathways of anthropogenic releases (Livingston and Povinec, 2002). The detection of ^{137}Cs, for instance, provides a definitive fingerprint of global fallout from mid 20th century atmospheric nuclear weapons testing, which serves as a widespread baseline for contamination (Aarkrog, 2003). Geophysicists and oceanographers integrate these radiometric maps with ocean current and sedimentological data to model the long term transport and sequestration of radioactive contaminants. A premier application of MGRS is the investigation of major accidental releases from events such as the Chernobyl and Fukushima Daiichi nuclear disasters. These events introduced significant quantities of ^{137}Cs, ^{90}Sr, and other isotopes into the marine environment, creating sharp and detectable anomalies that can be tracked over time and distance (Povinec et al., 2003). These anomalies act as a direct tracer for studying oceanic mixing processes, sediment accumulation rates, and biological uptake (Livingston and Povinec, 2002). Furthermore, MGRS contributes significantly to monitoring compliance and environmental impact assessment near nuclear facilities. Authorized, low level liquid discharges from nuclear reprocessing plants can create localized radiometric signatures that require careful distinction from global fallout. Similarly, the technique can be deployed to survey and locate submerged anthropogenic objects such as lost radioactive sources or sunken vessels with nuclear materials ((IAEA), I.A.E.A., IAEA-TECDOC-1363, 2003). By providing a unique window into the presence and behavior of human introduced radioactivity in the seafloor, MGRS is an essential component of international radiological surveillance and a powerful method for understanding the long term fate of anthropogenic contaminants in the marine environment.

It is worth mentioning that, MGRS also detects cosmogenic radionuclides, such as Beryllium-7 series, produced in the atmosphere by cosmic ray spallation (Lal and Peters, 1967). While their signal is often minor compared to primordial backgrounds, ^{7}Be short half-life (53.3 days) makes it a valuable tracer for studying recent sedimentation, particle adsorption, and short term mixing processes in the upper water column and surface sediments (Fitzgerald et al., 2001).

MGRS detects radiation anomalies that exhibit distinct spectral signatures, spatial distributions, and geological contexts, each indicative of different sources and implications. Various studies have been conducted in this field (Abdelhakim, 2025). Anthropogenic anomalies, characterized by isotopes like ^{137}Cs or ^{60}Co, typically arise from nuclear accidents, permitted discharges, or historical waste dumping. These point sources often display sharp concentration gradients and require monitoring due to their potential ecological and health impacts. In contrast, natural anomalies may reflect geological processes such as hydrothermal fluid venting, phosphate nodule deposits, or placer concentrations of heavy minerals like monazite (^{232}Th-rich) and zircon (^{238}U-rich). Such anomalies provide insights into sediment provenance, mineral resources, and active seafloor processes. Cosmogenic contributions including ^{7}Be are generally transient and homogeneous but may accumulate in depositional zones. Additionally, false anomalies can emerge from methodological artefacts such as radon gas fluctuations, changes in water depth, or equipment drift. Thus, accurate interpretation of MGRS data relies on discriminating between these sources through spectral analysis, spatial correlation with bathymetric or geological features, and

comparison with established baselines ((IAEA), I.A.E.A., IAEA-TECDOC-1363, 2003). These anomalies correlating their distribution not just with proximity to known sources, but with complex environmental parameters that govern their transport, sequestration, and detection. A primary correlation is established with oceanic current patterns and sediment logical parameters, as these directly control the advection and ultimate deposition of particle reactive radionuclides like ^{239}Pu isotopes and ^{137}Cs onto the seafloor (Periáñez, 2019). Crucially, atmospheric conditions including wind speed, direction, and humidity are key parameters correlated with the deposition and re-suspension of volatile radionuclides following atmospheric releases, directly influencing the initial input function and creating depositional anomalies (Hirose et al., 2008). Furthermore, oceanographic parameters such as water temperature and salinity are significantly correlated with the solubility, chemical speciation, and bioavailability of radionuclides, affecting their dispersion and incorporation into the marine food web (Povinec et al., 2003). Beyond physical transport, research correlates anomalies with bathymetric features; deep sea trenches and basins act as ultimate sinks, concentrating particulate bound radionuclides, while shallow shelves and slopes are prone to re suspension events driven by bottom currents (Sanchez-Cabeza and Ruiz-Fernández, 2012). Biological parameters are also critical, as high productivity zones can enhance the vertical flux of radionuclides through scavenging by phytoplankton and incorporation into biological pump processes, creating anomalies divorced from direct source input (Fisher et al., 2013). Methodologically, distinguishing a true seabed anomaly from a false signal requires correlation with *in situ* water depth and the overlying water column's attenuation properties, which directly impact the measured gamma-ray flux (Jones, 2001).

Advanced studies now integrate these correlations into sophisticated dispersion models, using multi parameter data to backtrack anomalies to their source, predict long term fate, and differentiate between the complex legacies of global fallout, regional accidents, and localized discharges (Periáñez, 2020). Numerous national and international programs are actively advancing ocean gamma spectrometry to monitor marine radioactivity, support environmental protection, and study oceanic processes. The global Marine Radioactivity Information System (MARIS), maintained by the IAEA, serves as a pivotal global database with over half a million measurements of radionuclides in seawater, biota, and sediments, enabling trend analysis and radiological assessments ((IAEA), 1991). These collaborative and standardized approaches, integrating data from diverse sources like nuclear facilities, scientific expeditions, and climate studies, are critical for understanding natural marine processes, assessing human impacts, and informing global policies on marine radiation safety.

Building upon this context and focusing on the complex marine settings of the Adriatic and Tyrrhenian Seas, this study addresses three sequential objectives: (1) to discriminate the source of semi persistent offshore gamma-ray anomalies along the Trieste to Aeolian Islands transects through spectral analysis; (2) to quantify correlations between these radiometric signatures and concomitant environmental and operational parameters, including bathymetry, meteorological factors, and vessel operational parameters; and (3) to initialize the foundational framework for a real-time diagnostic methodology. The implementation of this approach successfully differentiates between natural, anthropogenic, and instrumental sources, with results demonstrating strong agreement with discrete sample analyses literature. Critically, this integrated analysis enables, for the first time, the generation of a continuous map of radiometric variation along the survey track. This advancement provides a significant tool for radiological assessment and marine radiation protection. By prototyping a system for the synergistic, real-time processing of spectral and oceanographic data streams, this work transcends a case-specific analysis, offering a scalable framework to enhance operational monitoring, geophysical prospecting, and environmental baseline establishment in marine science.

2 Materials and methods

This section first presents the study area, encompassing the Adriatic Sea and Aeolian Islands. It then describes the R/V Laura Bassi and its radiation monitoring system, the primary data collection instrument. Following this, the theoretical framework underpinning the analysis is outlined. Subsequent subsections detail the data processing and spectral analysis methodology, define the flag radionuclides for each source category, and explain the statistical procedure for anomaly detection. Finally, the section concludes with an analysis of the associated measurement uncertainties.

2.1 Study area: a multi-source radionuclide environment from the Adriatic Sea to Aeolian Islands

This study investigates a diverse marine environment stretching from the land influenced waters of the northern Adriatic Sea to the volcanically active region surrounding the Aeolian Islands. This transect presents a unique opportunity to examine how different processes contribute to the presence of radionuclides in seawater. The aim is to establish a framework that considers not only the underlying geology but also a spectrum of potential sources, including hydrothermal venting, anthropogenic inputs, and cosmogenic production.

The Adriatic Sea itself is a semi enclosed basin, exhibiting strong latitudinal gradients. The northern Adriatic is shallow, with its northwestern end being only meters deep, and receives significant freshwater and sediment input from major rivers like the Po, which drains a large industrialized and agricultural watershed. In contrast, the southern Adriatic is deeper, with a maximum depth of more than one thousand meters in the South Adriatic Pit (SAP), and experiences greater influence of open ocean water masses from the Ionian Sea. These characteristics make the Adriatic highly sensitive to both terrestrial anthropogenic influences and natural oceanographic processes (Blake and Topalović, 1996).

At the southern end of this transect lies the Aeolian Islands, located at approximately southern of the Tyrrhenian Sea (Gabbianelli et al., 1990). Panarea is distinguished from its neighbors by its extensive submarine hydrothermal field,

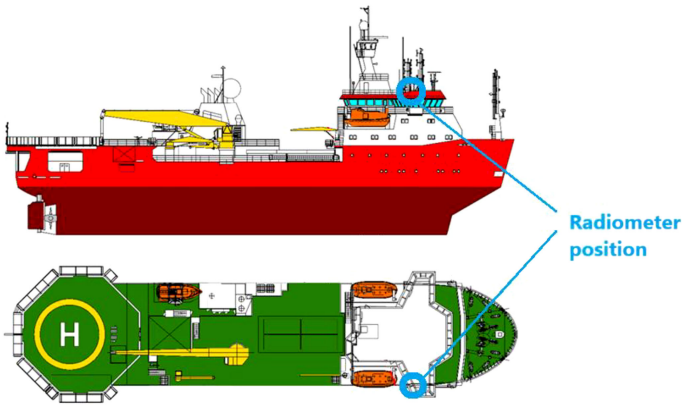

FIGURE 1
Installation of the RS-250 spectrometer.

characterized by gas vents and fumaroles, such as those near the village of Punta di Peppe e Maria and at Calcara beach, which alter the local seawater chemistry. This active venting is a significant point source for geogenic radionuclides, such as those from the Uranium and Thorium decay series. This island and entire Aeolian islands are a UNESCO World Heritage Site due to its outstanding volcanic features (Barreca et al., 2014).

The broader region is geodynamically active, resulting from the convergence of the African and Eurasian plates. The Aeolian Islands represent a volcanic arc, with the Lipari Vulcano complex being influenced by significant tectonic structures like the Aeolian Tindari Letojanni fault system. This tectonic setting provides the heat source and fluid pathways that sustain the hydrothermal activity observed around different Aeolian Islands.

Therefore, the area of investigation encapsulates a clear gradient from the stable, river dominated, and potentially anthropogenically influenced system of the Adriatic Sea to the dynamic, magmatically active point source at Aeolian Islands. This contrast is ideal for disentangling the signatures of diverse radionuclide sources, which will be explored in detail in the subsequent sections.

2.2 The R/V Laura Bassi and its radiation monitoring system

Routine monitoring of ambient gamma radiation was conducted using an RS-250 portable gamma-ray spectrometer (Radiation Solutions Inc.), operated with RadAssist (v6.2.83.0) and DgsAssist (v1.7.9.0) software. This instrument is a sodium iodide [NaI(Tl)]-based system designed for the *in-situ* identification and quantification of gamma-emitting radionuclides in environmental matrices.

For the present study, the spectrometer was deployed in a fixed-geometry configuration aboard the R/V Laura Bassi. The unit was permanently installed on the vessel's upper bridge deck as it is shown in Figure 1. This platform-mounted configuration facilitated continuous, long-term, route-based environmental surveillance. The primary objectives of this setup were: (1) to establish a baseline of ambient gamma radiation levels across the survey regions, and (2) to detect and characterize anomalous spectral signatures indicative of elevated atmospheric radioactivity or contamination events (Iurcev et al., 2025).

2.2.1 Gamma spectrometry system: instrument specifications and calibration

This subsection details the hardware, software, and calibration procedures to ensure traceable measurements.

- Detector: Thallium-doped sodium iodide [NaI(Tl)] scintillation crystal, 3 × 3 inches, coupled to a photomultiplier tube (PMT).
- Spectrometer Model: RS-250 (Radiation Solutions Inc.).
- Control & Analysis Software: RadAssist (v6.2.83.0), DgsAssist (v1.7.9.0), and OceTra (v1.1.2).
- Calibration & Certification: The full energy and dose rate calibration was performed by Radiation Solutions Inc. (Certificate No. 67-87570, July 14, 2023). Annual re-calibration is performed by the same company to maintain traceability.
- Calibration Source: Initial calibration has done by ^{137}Cs with activity 3.28 TBq/6.3 GBq source with calibration method of transfer standard and a 10 μCi point source of Novosal Hyposodic Salt (containing potassium at 28.5% enrichment) was used for routine energy calibration, verification of Full Width at Half Maximum (FWHM), peak fitting quality, and energy gain stability.
- Data Format: Spectra and data were recorded in both ANSI N42.42 and CSV formats.
- Integration with Vessel Systems: The spectrometer was connected to the ships internal network via Ethernet. Its integrated GPS was synchronized with the vessels primary GPS for spatial referencing.

It is worth mentioning that, to further support the reproducibility of such measurements, the raw data from an equivalent monitoring setup have been published in another article of team (Iurcev et al., 2025).

2.2.2 Measurement parameters and data acquisition

The primary radiometric variable analyzed is the Total Counts (TC), defined as the total gamma-ray counts accumulated over each 10-minute sampling interval.

For all measurements presented in this study, the spectrometer was operated with the following fixed parameters:

- Counting Time/Sampling Interval: 10 minutes per spectrum.
- Energy Range & Channels: The spectrum was recorded across 1024 channels, covering a full energy range from 0 to 3.072 MeV.
- Energy Resolution: Approximately 7–10% FWHM at 662 keV (~3 keV).
- Count Rate Limits: The system was set to record up to 50,000 counts per second, with a maximum of 1,000,000 counts per 10-minute sample.
- Sample Pretreatment Procedure: Not applicable. Measurements were conducted *in situ* on ambient marine aerosols without any physical sample collection or laboratory pretreatment. The reported activities are based on direct spectroscopic analysis of the airborne radionuclides intercepted by the detector.
- Output Units: Activity reported as counts per 10-minute sampling interval. Ambient dose rate reported in Gray per hour (Gy/h).

2.2.2.1 Parameters uncertainties

The analysis in this study is derived from radiometric data acquisition; consequently, all stated uncertainties originate from this process. The predominant source of uncertainty is the integration time of the spectrometer, which is 10 minutes for each measurement. All subsequent uncertainty calculations are based on this interval. It should be noted that overall analytical uncertainty can arise from both intrinsic instrument characteristics and the data collection methodology.

2.2.2.1.1 Latitude and longitude uncertainty

The positional uncertainty associated with each gamma-ray spectrum stems from the vessel's motion during the 10-minute acquisition window. The R/V *Laura Bassi* logs GPS positions (WGS84 datum) at one-minute intervals with centimeter-level precision. This specification is documented and certified in the vessel's technical manual; however, this manual is not available online. To access it, one must contact the manufacturer of the Kongsberg Seapath 380 (with MRU5) system directly to request the offline documentation for part number SEAPATH 380. However, as the radiometer integrates signal over a 10-minute period, the effective location of the measurement is ambiguous between the start and end points of this interval.

For a conservative (worst-case) estimate, the following assumptions are applied:

The vessel moves at its maximum operational speed of 13 knots (≈ 6.69 m/s).

The positional uncertainty is defined as the maximum possible displacement from the point selected to represent the integration period (here, the midpoint).

The vessel's GPS update interval (1 minute) contributes a negligible error relative to the displacement over 10 minutes.

Given a 10-minute integration, the maximum temporal offset from the representative midpoint is 5.5 minutes (5 minutes to the interval's start + 0.5 minutes for GPS timestamp alignment). The resulting maximum linear displacement is:

(5.5 min × 13 knots × 1.852 km/knot)/60 min/h ≈ 2.16 km.

Converting this to angular displacement (where 1° of latitude/longitude ≈ 111 km):

2.16 km/111 km/° ≈ 0.019°.

This is worth mentioning consideration, this conversion factor can vary in the different regions but this amount is effectively considerable in this working area.

Therefore, the estimated maximum positional uncertainty is ±0.019°. To conservatively account for this, reported coordinates are rounded to two decimal places of a degree.

2.2.2.1.2 Dose rate uncertainty

The uncertainty in the calculated ambient dose equivalent rate ($\dot{H}^*(10)$) originates from two primary sources: the intrinsic noise of the spectrometer and the uncertainty in the conversion from TC to dose rate. The instrument's inherent uncertainty is defined by the manufacturer's specifications (RS-250 catalogue). An additional systematic uncertainty arises from the application of the energy-dependent conversion coefficients (Liu et al., 2022). Based on a synthesis of these factors, a combined standard uncertainty of 1 nSv h^{-1} is assigned to the reported dose rates for gamma-ray measurements.

2.2.2.2 Ancillary meteorological measurement parameters

To investigate correlations between atmospheric conditions and radiation variations, continuous meteorological data were collected aboard the Laura Bassi using a Vaisala WXT530 Series Weather Transmitter. This instrument provides high-resolution, co-located measurements of key atmospheric variables that influence aerosol transport, cloud formation, and air density all factors affecting ambient radiation fields.

The fixed operational parameters and measurement specifications for each variable are as follows (Oyj, 2023):

2.2.2.2.1 Wind

Wind dynamics influence the advection and dispersion of radionuclide-carrying aerosols. The sensor reports:

Speed: Resolution of 0.1 m/s, within a range of 0–60 m/s (reportable up to 75 m/s).

Direction: Resolution of 1°, across a full azimuth range of 0–360°.

2.2.2.2.2 Atmospheric pressure

Pressure is a key indicator of synoptic weather systems and affects air density, which in turn influences gamma-ray attenuation. The sensor measures:

Resolution: 0.1 hPa.

Range: 500 to 1100 hPa.

2.2.2.2.3 Air temperature

Temperature profiles affect atmospheric stability and convective mixing, which can alter near-surface radionuclide concentrations. The sensor provides:

Resolution: 0.1°C (or 0.1°F).

Range: −52 to +60°C (−60 to +140°F).

2.2.2.2.4 Relative humidity

Humidity affects both aerosol particle size and the attenuation of low-energy gamma rays. The sensor measures:

Resolution: 0.1% RH.

Range: 0 to 100% RH (Oyj, 2023).

All parameters were recorded synchronously with radiometric data at configurable intervals, enabling time-series analysis of meteorological influences on observed radiation levels.

2.2.3 Data recording research cruise legs

The data collection for this study was conducted during the 2024–2025 Antarctic campaign, the 2025 Summer campaign, and the 2025 Antarctic campaign expeditions aboard the R/V Laura Bassi. These campaigns were structured into four distinct legs:

- Leg 0: 15th - 19th April, from Aeolian Islands to Trieste.
- Leg 1: 26th August - 4th September, from Trieste to Aeolian Islands.
- Leg 2: 5th - 15th September, Aeolian Islands to Trieste.
- Leg 3: 4th Oct - 9th November, from Trieste to Aeolian Islands.

The geographical tracks of all four legs are illustrated in Figures 2–6, providing a visual representation of the spatial coverage.

2.3 Theoretical framework for anomaly interpretation

This section outlines the theoretical framework developed to interpret the observed anomalies in the detector's count rate. The model conceptualizes the detected signal as a function of three sequential physical processes: 1) the spatial and temporal distribution of radionuclides within the detector's effective field of view; 2) the transport of gamma-rays from the source to the detector through a variable medium; and 3) the final interaction within the detector and its subsequent response. The formulations are developed with a focus on the key environmental and operational parameters present in this research, deliberately setting aside secondary effects for clarity.

2.3.1 Spatial and temporal distribution of radionuclide sources

The primary source of the detected signal is the concentration of radionuclides within the detector's effective window, defined by its solid angle and the effective penetration depth of gamma-rays in the medium (air, metal and water). The total contribution is modeled by discretizing this volume into a 3D grid and summing the activity of all radionuclides across all grid cells. The general form of the total concentration is given by Equation 1:

$$C^{total} = \sum_{i=1}^{N}\sum_{x=1}^{L}\sum_{y=1}^{M}\sum_{z=1}^{k} C(i,x,y,z) \quad (1)$$

where:

- i is the index of the radionuclide type.
- x, y, z, are the discrete grid coordinates.

C(i, x, y, z) is the concentration of radionuclide i in grid cell (x, y, z).

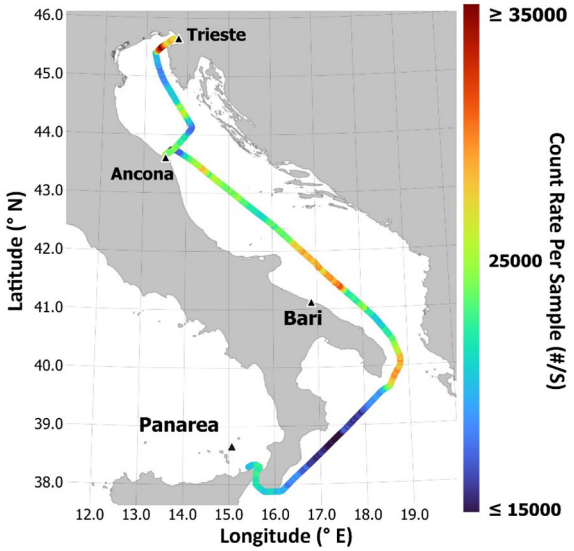

FIGURE 2
Radiation survey map with anomalies in leg 0.

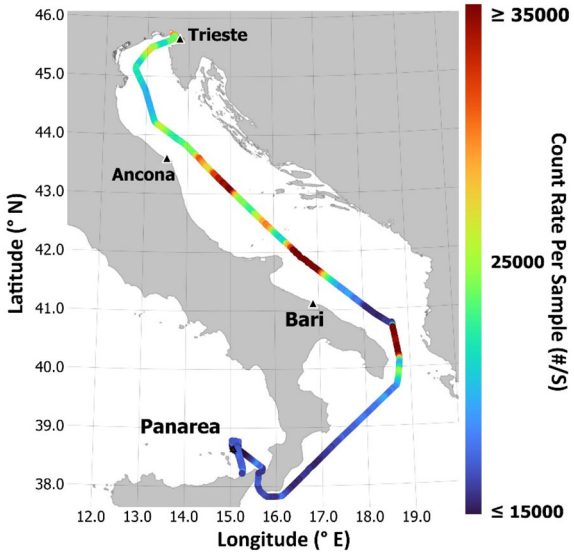

FIGURE 3
Radiation survey map with anomalies in Leg 1.

10.3389/fmars.2026.1750403

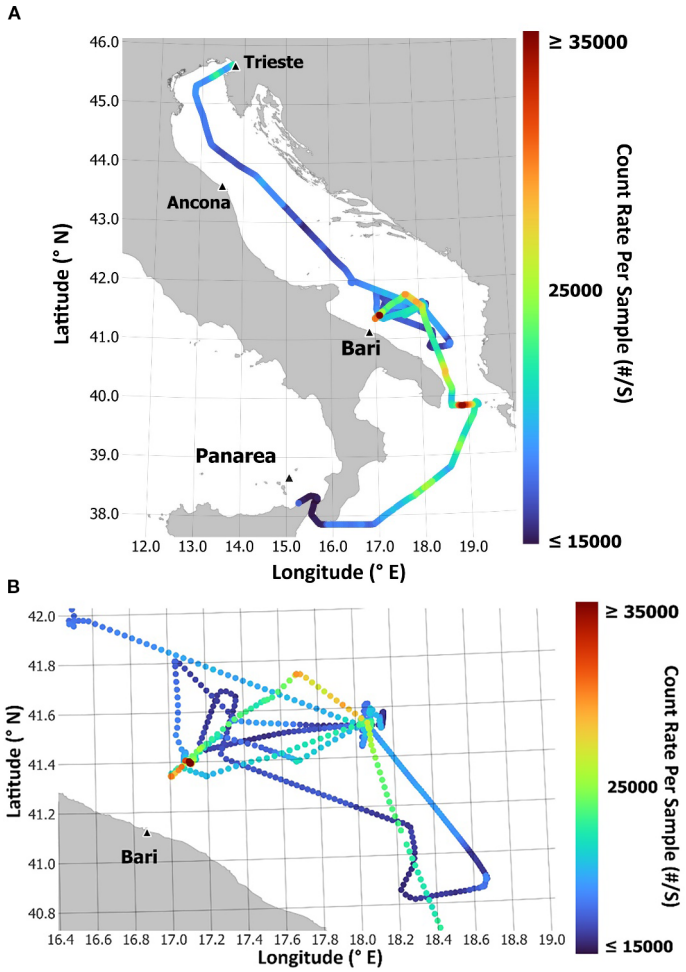

FIGURE 4
Radiation survey map with anomalies in leg 2, **(A)** Overall path, **(B)** Spaghetti section.

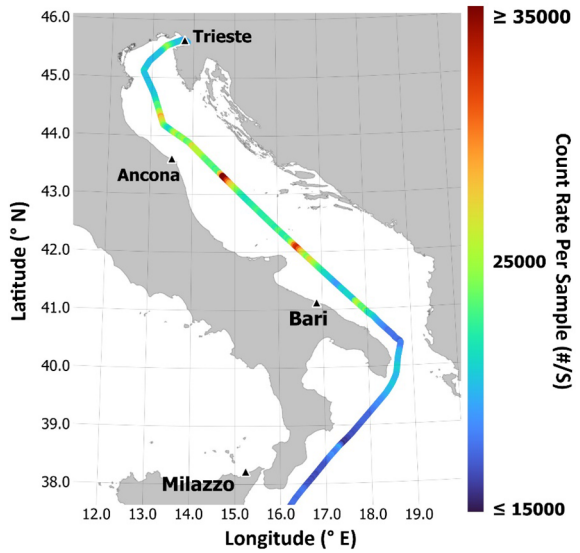

FIGURE 5
Radiation survey map with anomalies in leg 3.

It is critical to note that the detected signal originates not only from the primary photopeak emissions of each source but also includes significant contributions from other gamma energy levels, particularly from Compton scattering events and even gamma levels with less hindrance factor.

To model the dynamic behavior, the rate of change of concentration for a specific radionuclide in a given grid cell i is governed by a differential equation (Equation 2) that accounts for transport and decay:

$$\frac{dC_i}{dt} = \sum_{j=1}^{n} k_{ji} C_j - \sum_{j=1}^{n} k_{ij} C_i - \lambda_i C_i e^{-\lambda_i t} + f_{ji} \lambda_j C_j e^{-\lambda_j t} \quad (2)$$

where:

- The first two terms represent the transport into and out of cell i, with rate constants k.
- The third term is the radioactive decay of radionuclide i.
- The fourth term represents the ingrowth from the decay of parent radionuclides j.

A key dependency in this model is the influence of environmental advection on the transport rate constants. For

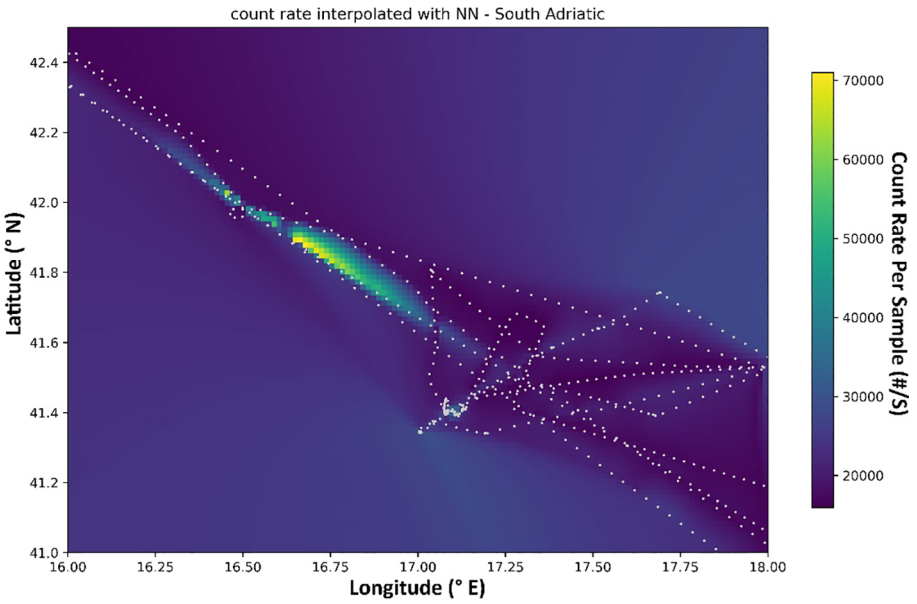

FIGURE 6
Radiation survey map interpolation in anomaly region.

instance, over short timescales, wind speed and direction are the primary drivers, such that (Equation 3):

$$\begin{cases} k_{ij}(wind) \\ k_{ji}(wind) \end{cases} \tag{3}$$

While parameters like humidity, temperature, and depth do not appear directly in Equation 2, their influence is critical as boundary conditions. They govern the physical processes of injection and ejection of radionuclides at the interfaces of the system including sea-to-air flux, and sedimentation.

2.3.2 Gamma-ray transport: scattering and attenuation

As gamma-rays travel from their source to the detector, they are subject to scattering and absorption. The intensity I of a collimated beam of gamma-rays after traversing a distance d in a homogeneous medium is given by the Beer-Lambert law (Equation 4):

$$I = I_0 e^{-(\mu/\rho)d} \tag{4}$$

- where: I_0 is the initial intensity at the source.
- μ/ρ is the mass attenuation coefficient (cm^2/g).
- d is the areal density (g/cm^2), often written as ρ_d, where ρ is the material density.

The total linear attenuation coefficient μ is derived from the sum of individual interaction cross-sections per atom (Equations 5, 6):

$$\frac{\mu}{\rho} = \sigma_{tot}/uA \tag{5}$$

$$\sigma_{tot} = \sigma_{pe} + \sigma_{coh} + \sigma_{incoh} + \sigma_{pair} + \sigma_{trip} + \sigma_{ph.n.} \tag{6}$$

Where σ_{pe} is the atomic photoeffect cross section, σ_{coh} and σ_{incoh} are the coherent (Rayleigh) and the incoherent (Compton) scattering cross sections, respectively, σ_{pair} and σ_{trip} are the cross sections for electron-positron production in the fields of the nucleus and of the atomic electrons, respectively, and $\sigma_{ph.n.}$ is the photonuclear cross section.

In the real environment, the path between a source grid cell and the detector is a mixture of air, water, and vessel structures. The total attenuation is therefore the sum of the contributions from each material (Equation 7):

$$I = I_0 e^{-\sum_{i=1}^{N}(\mu_i/\rho_i)d_i} \tag{7}$$

Here, environmental conditions such as temperature and humidity exert a significant indirect influence. They alter the density (ρ) of the air and, to a lesser extent, water, thereby modifying the areal density (ρ_d) and the overall attenuation along the path (Krane, 1991).

2.3.3 Detector response and final count rate synthesis

The final stage of the model accounts for the detector's response. The measured total gamma-ray counts accumulated over each 10-minute sampling interval (TC) is not a direct measure of the incident radiation field but a complex signal shaped by the detector's intrinsic physics and its operational environment. The $TC_{Detector}$ can be conceptualized as Equation 8:

$$TC_{Detector} = TC_{Real} + TC_{Artifacts} \tag{8}$$

Where:

TC_{Real} is the desired signal originating from the natural radioelement concentrations including Potassium, Uranium,

Thorium series, also possible anthropogenic radionuclides including Cesium and Cobalt series in the study area.

$TC_{Artifacts}$ encompasses all confounding factors, including instrumental nonlinearities (such as pulse pileup and dead time) and also environmental condition effects on detector response (such as temperature and humidity) which is claimed compensated by producer.

The performance of the detector material itself is largely governed by the physics described by the attenuation coefficients, which determine the probability of a gamma-ray interacting within the detector crystal to produce a countable pulse (Knoll, 2010).

2.3.4 Synthesis of theoretical contributions

The correlation between environmental parameters wind, temperature, depth, and humidity and the total recorded TC is not governed by a single mechanism. Instead, it emerges from the combined and sequential influence of these parameters on the coefficients within the integrated model. So what will be seen in the 4.4 Correlation with Bathymetric and other Features, will show overall affect not only one part.

2.4 Data processing and spectral analysis methodology

2.4.1 Raw data extraction from N42 files and pre-processing

The extraction of spectral channel data is performed in compliance with the certified ANSI/IEEE N42.42 data format standard. For the purposes of this work, a dedicated C code module was developed to parse the N42 XML structure and retrieve all measurement parameters. The core routine locates the <ChannelData> element, whose textual content contains the raw, space-separated spectrum. A critical implementation detail is handling the optional compressionCode="CountedZeroes" attribute, which signifies that consecutive zero-count channels are run-length encoded for example "0 5" denotes five zero-count channels.

Concurrently, the module extracts essential metadata from sibling elements, including timing information, geographical coordinates, and energy calibration coefficients. The integrity of the extraction process requires careful consideration of the N42.42 schema definitions to ensure all data relationships are preserved and correctly interpreted.

This process yielded, for each 10-minute measurement, a 1024-channel array of raw counts and its associated metadata (timestamp, GPS coordinates).

2.4.2 Energy calibration and spectrum stabilization

The extracted raw channel data were converted from channel number to energy (keV) using the linear calibration coefficients (Energy = a × Channel + b) derived from the instrument's annual calibration and verified daily using the onboard ^{40}K check source. A background reference spectrum, representative of open-sea conditions away from identified anomalies, was averaged from multiple recordings and subtracted from each measured spectrum to remove the contribution of the instrument's intrinsic background and constant cosmic component.

2.4.3 Spectral analysis and radionuclide quantification

Peak identification: Photopeaks in the background-corrected spectra were identified using a first-derivative peak search algorithm, focusing on the characteristic energies of the flag radionuclides including 609.3 keV for ^{214}Bi, 1460.8 keV for ^{40}K, 661.7 keV for ^{137}Cs.

Net peak area calculation: For each identified photopeak, the net photopeak counts (NnetNnet) were calculated using Equation 9:

$$N_{net} = N_{gross} - N_{bg} \tag{9}$$

where:

N_{gross} = total counts within the photopeak's Region of Interest (ROI).

N_{bg} = estimated background counts under the photopeak, modeled from the adjacent Compton continuum via linear interpolation between ROI boundaries.

Signal-to-noise ratio (SNR) determination:

The statistical significance of a radionuclide detection was evaluated using its Signal-to-Noise Ratio (SNR). In accordance with Currie's detection limits for gamma-ray spectrometry, the SNR was calculated using Equation 10:

$$SNR = N_{net}/\sigma_{N_{net}} \tag{10}$$

where $\sigma_{N_{net}}$ is the standard deviation of the net photopeak counts. Under Poisson statistics, this uncertainty is expressed using Equation 11:

$$\sigma_{N_{net}} = \sqrt{N_{bg} + N_{gross}} \tag{11}$$

Thus, the SNR simplifies to Equation 12:

$$SNR = \frac{N_{net}}{\sqrt{N_{bg} + N_{gross}}} = \frac{N_{gross} - N_{bg}}{\sqrt{N_{bg} + N_{gross}}} \tag{12}$$

A detection was considered statistically significant for SNR ≥ 3, corresponding to a confidence level exceeding 99.7% under the assumption of normal distribution for net counts.

2.4.4 Correlation with environmental parameters

The TC and flag radionuclide net count rates per sampling time were synchronized with co-located bathymetric and meteorological data (wind speed, air temperature, relative humidity) using UTC timestamps. Linear Pearson correlation coefficients (r) and the coefficient of determination (R^2) were calculated to quantify the relationship between radiometric variables and each environmental parameter.

2.4.5 Pearson correlation formula

The linear Pearson correlation coefficient γ between two synchronized variables x for example a TC and y for example an

environmental parameter such as wind speed for n paired observations was calculated using Equation 13:

$$\gamma_{xy} = \frac{\sum_{i=1}^{n}(x_i - \bar{x})(y_i - \bar{y})}{\sqrt{\sum_{i=1}^{n}(x_i - \bar{x})^2 (y_i - \bar{y})^2}} \quad (13)$$

Where:

x_i and y_i are the individual sample points (synchronized by UTC timestamp) indexed by *i*.

$\bar{x}$ and $\bar{y}$ are the sample means of the radiometric variable and the environmental parameter, respectively.

n is the number of paired samples.

The coefficient of determination R^2 was subsequently derived as $R^2 = r_{xy}^2$, representing the proportion of variance in the radiometric signal explained by the linear relationship with the environmental parameter (Pearson, [[NoYear]]).

2.5 Flag radionuclides

The identification of specific "flag radionuclides" is fundamental to interpreting *in-situ* Gamma-ray spectra in the marine environment. These radionuclides serve as unique fingerprints, allowing for the immediate classification of detected radiation into its source of origin: natural terrestrial processes, human activities, or cosmogenic production. For a NaI(Tl) scintillator positioned on the upper deck of vessel, the measured spectrum is a composite of signals from atmospheric aerosols, sea spray, and ambient background radiation. The following subsections detail the key gamma-emitting radionuclides within each category that are most relevant for this measurement geometry.

2.5.1 Natural radionuclide flags

The natural Gamma-ray background is dominated by the primordial decay chains of Uranium and Thorium, along with the ubiquitous Potassium. The most prominent spectral features originate not from the parent nuclides themselves, but from their short-lived progeny, which become airborne through the emanation of radon gas ^{222}Rn and ^{220}Rn and the suspension of dust and sea spray. The primary flag for the Uranium series is the pair ^{214}Bi, with its distinct 609.3 keV gamma line, and ^{214}Pb, emitting at 351.9 keV. For the Thorium series, ^{208}Tl is a key flag, identified by its 583.2 keV and high-energy 2614.5 keV emissions. The presence of the natural background is semi-consistently confirmed by the 1460.8 keV gamma-ray from ^{40}K.

2.5.2 Anthropogenic radionuclide flags

Anthropogenic radionuclides are human-made and indicate the presence of contamination from nuclear weapons testing, nuclear accidents, or industrial releases. Their detection in the marine atmosphere is a clear signature of such activities. The most significant and persistent anthropogenic flag is ^{137}Cs, which emits a characteristic gamma-ray at 661.7 keV. Its presence is often a direct indicator of global fallout or specific incident releases. In the event of a recent release, ^{134}Cs, with its 604.7 and 795.8 keV emissions, and ^{131}I, with a dominant 364.5 keV gamma-ray, serve as critical short-term flags. The detection of any of these nuclides above background levels warrants further investigation into their source.

2.5.3 Cosmogenic radionuclide flags

Cosmogenic radionuclides are produced continuously in the upper atmosphere by the interaction of cosmic rays with atomic nuclei. They are useful as tracers for atmospheric circulation and mixing processes. The most readily detectable cosmogenic flag with a gamma spectrometer is Beryllium-7 (^{7}Be). It has a half-life of 53.3 days and produces a well-defined gamma peak at 477.6 keV, making it a common and identifiable feature in spectra from air filters and atmospheric measurements. While other cosmogenic radionuclides like ^{14}C or ^{10}Be are highly relevant in oceanography, they are pure beta emitters and are not detectable with gamma spectrometry, thus falling outside the scope of this *in-situ* measurement technique (Povinec et al., 2008; Lee, 2017).

2.6 Statistical definition and detection of gamma-ray anomalies

In this study, a gamma radiation anomaly is quantitatively defined as a statistically significant elevation above the local, natural background. Given the established variability in background radiation across different marine regions, employing a single global threshold is inappropriate. Therefore, a dynamic, moving-window statistical approach was implemented to calculate anomaly thresholds specific to each geographical area. The procedure for defining and identifying anomalies consisted of three key steps as it its flowchart shown in the Figure 7:

The rationale for selecting the numbers 5 and 30 is that, according to references citing the main article from Currie (1968) (these references do not establish a universal rule but rather share a common empirical approach), the best method for identifying

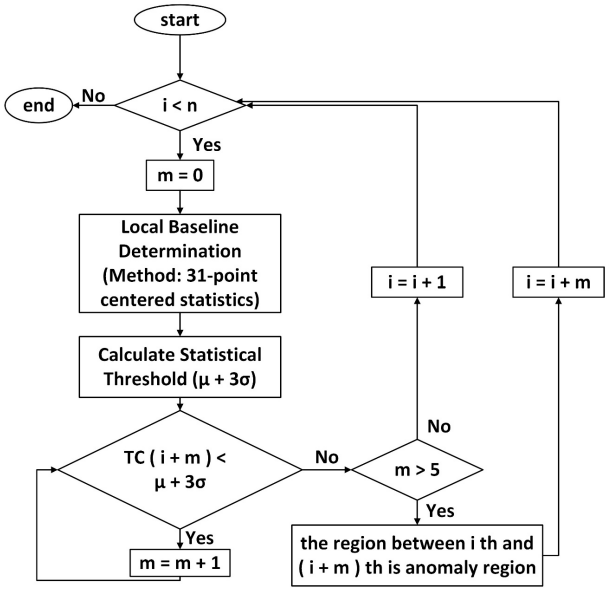

FIGURE 7
Anomalies detection flowchart.

anomaly regions is to first find the location of region with the highest anomalies and then consider 50–70% of that anomalous area extent as the minimum anomaly extent threshold (to remove noise effects, etc.), and then consider average of value in 5 to 10 times bigger area as the background mean.

In this study, given that after plotting the heatmap this value was 8, which multiplied by 10–12 knots of Laura bassi speed (approximately divided by 6, since sampling occurs every ten minutes) and by 1.852, yields a value between 25 and 29 kilometers. Consequently, the minimum width of the anomaly region could be adopted as 12 to 20 km, and the background mean used could have range from 60 to 200 km. In this research, 12 km (approximately 5 consecutive data points) and 100 km (approximately 30 consecutive data points) were selected. In areas where the data were intertwined, where multiple passes were made such as in the southern Adriatic during the second voyage the same 12 km and 100 km were used as the radius for the anomaly range and the mean, respectively, instead of the count of consecutive data points. During averaging, only the data that were utilized were used as the criterion for the mean, and, for example, data points closer to coastal areas even within the 100 km radius were omitted from the analysis.

2.6.1 Establishment of local background statistics

For each measurement point, the local background mean (μ) was calculated using a dynamic, distance-based moving window. The background area was defined by a radius of 100 km (approximately 30 consecutive data points along the vessel's track). Within this radius, data points in close proximity to coastal areas or other known anthropogenic influences were excluded to ensure the background represented the open-sea natural variability. From this curated background dataset, the local standard deviation (σ) was computed using the formula:

$$\sigma = \sqrt{\sum_i \frac{(TC_i - \mu)^2}{N - 1}} \tag{14}$$

where TC_i is an individual measurement, μ is the local mean, and N is the sample count. Preliminary extreme outliers were excluded prior to this calculation to prevent inflation of σ.

2.6.2 Application of the statistical threshold

A measurement was flagged as a potential anomaly if its TC_i satisfied the condition:

$$TC_i > \mu + 3\sigma \tag{15}$$

The multiplier n=3 defines a high confidence level, corresponding to a less than 0.3% probability that such a value belongs to the normal background distribution under Gaussian assumptions. This method follows established principles for discriminating weak signals from variable backgrounds in radiation measurement.

2.6.3 Identification of persistent anomaly regions

Spatially contiguous flagged anomaly points were grouped. To distinguish a persistent offshore anomaly from transient noise, a candidate anomaly region was required to have a minimum spatial extent of approximately 12 km (derived from ~5 consecutive data points). Furthermore, for a region to be classified as a principal finding a stable component of the marine environment it had to be identified across two or more independent cruise legs. This multi-leg confirmation ensures the feature is not an artifact of specific atmospheric or vessel conditions.

2.6.4 Workflow example from the central Adriatic dataset

In a region where the dynamic background calculation for a 100 km radius yields μ ≈ 3000 TC and σ ≈ 300 TC, the anomaly threshold is: $\mu + 3\sigma = 3000 + (3 \times 300) = 3900$ TC. A measured value of ~12,000 TC, being approximately four times the local mean and vastly exceeding this threshold, is robustly identified as a significant statistical anomaly. This initial detection then triggers the detailed spectral analysis to determine the radionuclide source.

3 Results

The Results section begins with an overview of the acquired radiometric dataset, providing a definition and general description of the data. Subsequently, the TC variation is analyzed, and anomalous points are identified to highlight regions of potential anomalies. The spectral variations of these anomalous points are then examined to investigate the possible radionuclide sources. Following this, correlations with bathymetric and other environmental features are explored. Finally, the analysis is concluded with a comparison to previous studies, an interpretation of the potential natural sources of the anomalies, and a concise summary synthesizing the main findings.

3.1 Overview of the acquired radiometric dataset

The gamma-ray spectrum shown in Figure 8 was obtained by summing the total counts over the entire 10 minute acquisition time for each sample. The distribution of counts as a function of energy channel is displayed, with the x axis representing the energy calibration and the y axis the measured TC. Although the primary data were processed from the N42 files, equivalent data can be derived from the corresponding.csv exports. Subsequent analysis of these spectra allows for the determination of the total absorbed dose rate and the apportionment of dose contributions from identified radionuclides.

3.2 TC variation and anomaly point finding

This section analyzes several marine anomaly regions that demonstrated remarkable persistence across all four cruise legs. This semi-consistency is particularly significant given that the legs occurred under varying environmental and vessel conditions, including different ship speeds, headings, temperatures, and wind patterns.

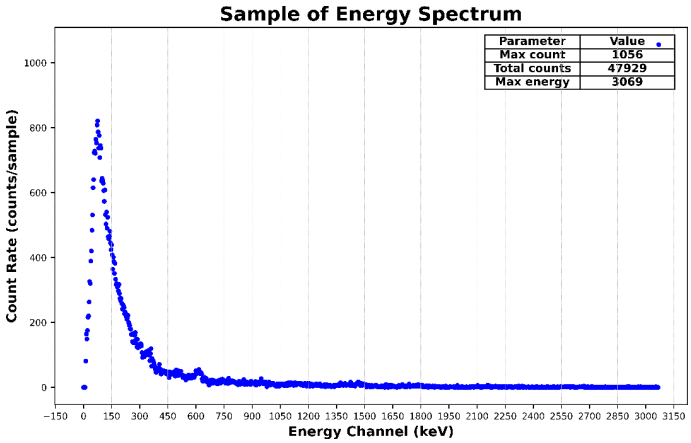

FIGURE 8
Typical gamma-ray energy spectrum of the instrument.

While the exact geographic coordinates of the anomalies central points shifted slightly due to these dynamic conditions, the specific region in which it occurred remained semi-consistently fixed. Furthermore, the quantity and intensity of acoustic peaks within these regions varied between legs; however, the occurrence of localized peaks was a certain and reproducible feature.

The four figures referenced below (Figures 2–5) present the data numerically for Legs 0 - 3, as defined in Section 3.2.1. The most prominent radiation TC peaks identified within these persistent regions are quantified and detailed in Table 1 of this section.

The Figure 2 presents the radiation survey map for Leg 0, revealing three prominent anomalies located in the northern, and central Adriatic Sea, as well as Strait of Otranto. These anomalies are distinctly identified by an orange to red color gradient, indicating elevated radiation levels.

A key characteristic of these anomalies is their spatial structure. The radiation levels in the surrounding areas, even at distances of ten kilometers or more, do not drop abruptly. Instead, they exhibit a gradual decrease. This persistent signal, as emphasized by the data processing algorithm, confirms that the anomalies are not transient artifacts or instrumental noise. Furthermore, this broad spatial continuity suggests that the source of the radiation is not a highly localized point source, but rather indicative of a more widespread distribution or a regional process.

Figure 3, which presents the radiation survey data for Leg 1, confirms the persistence of the anomalous regions identified in Leg 0. It reveals peaks in geographically similar areas of the Adriatic Sea. However, the precise geographic coordinates of these peaks show slight variation, and their measured intensity values differ from those recorded in the previous leg. This observed variability aligns with the dynamic environmental and vessel conditions documented across the cruise legs, further supporting the conclusion that these are persistent regional features rather than instrument artifacts.

Figures 4A, B exhibits a similar pattern of anomalies, corroborating the findings from the preceding legs. The strategic importance of Leg 2's data is its survey design, which involved multiple round trip routes across the region. This dense data collection strategy which is seen in figure a has focused as a spaghetti section in the b was deliberately implemented to investigate the suspected anomaly regions further.

The high resolution track lines from Leg 2 were crucial for the reconstruction and interpolation process, directly enabling the creation of the comprehensive map in Figure 6. In essence, this specific segment of the cruise was dedicated to targeted data collection to refine and consolidate the existing evidence for these persistent anomalies.

Figure 5 presents the data from the final cruise leg (Leg 3), representing the most recent transit of the R/V Laura Bassi through the study region. The results confirm the prior observations, with anomalies clearly present in geographically semi-consistent areas. The repeated detection of these features across all four independent legs, under varying conditions, provides robust validation of their persistent nature.

Figure 6 presents a spatially interpolated radiation survey map focused on one of the persistent anomalies, specifically the one located in the central Adriatic Sea. The interpolation method is the natural neighbors or Sibson's method, which use the geometrical properties of the Voronoi decomposition (Iurcev et al., 2021). This composite visualization integrates the data from all four cruise legs. As the map clearly demonstrates, the interpolation process synthesizes this multi leg dataset to reveal a well defined and coherent anomalous region, confirming its spatial semi-consistency and significance.

The central coordinates for each of these three anomalous regions and Aeolian islands as a sample of normal point, representing the point of highest TC within each area, are detailed in Table 1.

TABLE 1 Key anomaly coordinates.

Anomaly region	Latitude	Longitude	Sample tc
Central Adriatic Sea	43.09 N	14.96 E	34,659
Southern Adriatic Sea	41.98 N	16.50 E	76,854
Strait of Otranto	40.15 N	18.60 E	32,415
Aeolian Islands	38.70 N	15.08 E	15,176

The final interpretation regarding the origin and significance of these persistent offshore anomalies is presented in the section titled 4.6 Interpretation.

3.3 Spectrum variations of anomalous points

As detailed in the previous section, three distinct anomalous regions were identified based on elevated TC. This section presents a detailed analysis of the Gamma-ray energy spectra collected at these specific coordinates to investigate the radionuclide composition responsible for the observed anomalies. Although the exact coordinates of these points are listed in Table 1, as described in Section 4.2, these points represent temporary data recording locations and cannot be considered fixed latitude and longitude coordinates.

Analysis of the Gamma-ray spectra from the anomalous points, presented in Figure 9, reveals distinct photopeaks that were identified as key radionuclides flags. The most prominent peaks were identified as characteristic gamma emissions from radionuclides within the natural Thorium and Uranium decay series.

As shown in Figure 9, the key identifiers include:

- Peaks A and B at approximately 80–120 keV, which are mostly related to X-rays.
- Peak C at around 186 keV, corresponding to ^{226}Ra.
- Peak D at nearly 300 keV, which could be due to either ^{214}Bi or ^{208}Tl.
- Peak E at around 360 keV, possibly from ^{214}Pb or ^{214}Bi.
- Peak F at 609 keV, corresponding to ^{214}Bi.
- Peak G at approximately 770 keV, ^{214}Bi.
- Peak H at 930 keV, ^{214}Bi.
- Peak I at around 1120 keV, ^{214}Bi.
- Peak J at approximately 1260 keV, ^{214}Bi.
- Peak K at nearly 1410 keV,
- Peak L at 1746 keV, ^{214}Bi.

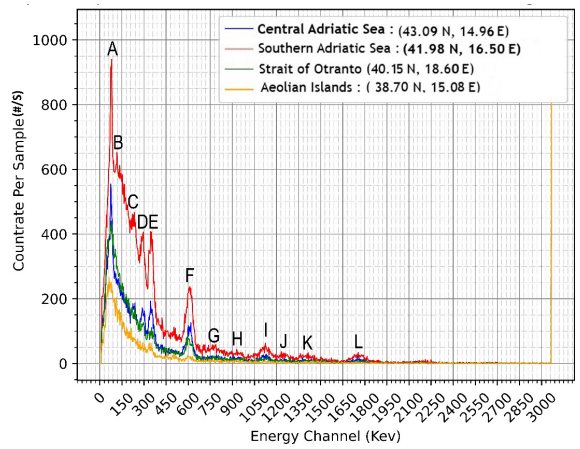

FIGURE 9
Gamma-ray spectra from identified anomaly regions.

The analysis focused on these high probability, high intensity emissions from common marine radionuclides; Low intensity peaks or subtle spectral variations in the low energy region were not investigated. The potential presence of each radionuclide in ocean and seawater samples was considered, and the spectral analysis was performed using a specialized library derived from the Evaluated Nuclear Structure Data File (ENSDF) database, maintained by the International Atomic Energy Agency (IAEA) and the National Nuclear Data Center (NNDC) (Bhat, 1992), taking into account the probability of each radionuclide, its decay, and the likelihood of its characteristic energy peaks. A specified flagged peak energy has a perfect match with the described spectrum of the RS-250. As declared, the energy peak below 100 keV is part of the background and is related to internal scatter, backscatter, and x-ray reflections in background. The spectral feature in the 100–300 keV region is primarily a smooth continuum from Compton scattering, which is generally negligible for radionuclide identification. Other minor peaks in this area correspond to less prominent gamma emissions (which are specified in the ENSDF data sets as energy levels with a very high or very low hindrance factor) or scattering events with a lower cross section of interaction (which are specified in the ENDF/B data sets) (Bé et al., 2004; Brown, 2018; Giraldo and Ramírez, 2023).

A notable point is that ^{226}Ra and its daughter ^{214}Bi in the decay chain are the most prominent. Another important point is that there can be peaks close to the ^{214}Bi peaks, but they are interpreted as ^{214}Bi because the full spectrum of this radionuclide is present. Although similar peaks exist for ^{152}Eu and other radionuclides, there is no complete spectrum including all parent isotopes and all characteristic energy peaks to support their presence. Given the low likelihood of unrecorded human related activities in these regions, the data predominantly indicate natural sources. However, this does not rule out the possibility of anthropogenic radionuclides being present.

3.3.1 SNR consideration

With considering full expected spectrum for each radionuclide and calculating possibility and SNR of existence of each one in solution including all one Table 2 is calculated. It is clear these numbers are not rigid and could change with varying percentage of each one and even composition of radionucluides.

But important parameter is in such prediction, possibility of all natural radionuclides are high, in order of more than ten and for anthropogenic ones its less than one or even minus, which is

TABLE 2 SNR calculation for estimated composition.

Radionuclide (Series)	Category	SNR
^{226}Ra (Uranium)	Natural	11.855
^{232}Th (Thorium)	Natural	4.505
^{40}K (Potassium)	Natural	11.614
Cosmogenic	Natural	13.251
^{137}Cs decay series	Anthropogenic	0.174
^{60}Co decay series	Anthropogenic	0.023

meaning these are less possible and their affect is comparable with noise and negligible.

Table 2 show the SNR in related energy channels in the biggest peak:

3.4 Correlation with bathymetric and other features

This subsection investigates the correlation between the observed radiological variations (TC and spectral features) and key accessible environmental parameters: bathymetry, wind speed, and ambient temperature. The influence of these factors on the distribution and detection of natural radionuclides have been analyzed.

3.4.1 Bathymetry

Bathymetry is a critical parameter in this context, as it directly influences the concentration of radionuclides in the water column, and distributed in the atmosphere and consequently seen by spectrometer. Shallow coastal areas, particularly near ports and industrial sites, can exhibit elevated radiation levels due to several factors: the resuspension of seabed sediments containing natural radionuclides, limited water volume for the dilution of discharges, and potential contributions from industrial activities. These factors can significantly affect both acquired data and spectral shapes. However, the focus of this research is explicitly on the off shore sea and ocean environment. Consequently, anomalous points identified in close proximity to coastal regions and port facilities were excluded from this analysis. This ensures that the investigated anomalies are representative of offshore processes and are not confounded by localized terrestrial or anthropogenic inputs from land based sources.

The relationship between water depth and radiation TC was investigated in Figures 10, 11. Figure 11 confirms an overall inverse correlation between depth and TC, as expected, where the measured TC generally decreases with increasing depth.

However, this general rule is not the dominant factor in the identified offshore anomaly regions. As clearly shown in the time series trends of Figure 10, this inverse relationship is not consistently followed at all data points. The visual map further reveals that within the specific anomaly areas, the TC remains high or even increases despite constant or increasing depth.

In summary, while an inverse depth correlation with TC exists as a background trend, it is not the primary cause of the observed anomalies. This correlation alone cannot explain the persistent high TC features, indicating that another source or mechanism is responsible for their occurrence.

3.4.2 Wind

The effect of these wind related mechanisms was investigated in relation to the observed data, as presented in Figures 12, 13. Figure 12 displays the time trend of normalized wind speed and TC, while Figure 13 illustrates the correlation between these two parameters. While wind is a prominent factor influencing radiation measurements, its role is complex. It affects readings by increasing sea spray aerosols carrying oceanic radionuclides and by transporting distant terrestrial materials. These mechanisms can alter the local radiological signature. However, the analysis concludes that wind's explanatory power for temporal variations is not easily to configure, specially it is important to now direction of wind and speed of vessel along with land position. Generally, for the identified semi-consistent anomalies those semi-persistent across multiple research legs wind patterns alone cannot fully account for the sustained elevation in radiation levels. This suggests that while wind may act as a transient modifier, the source cause of these semi-consistent anomalies is likely a stable, localized source, such as a seabed emission or a concentrated hydrological feature, whose signal is robust against short term meteorological variations.

In summary, wind plays a role in modulating the atmospheric concentration of radionuclides, but it is not the dominant driver of the most significant and persistent anomalous features detected in this study.

Regarding wind, there is another important issue related to its direction. Wind is not only a scalar quantity; its direction significantly affects the results. This is important because wind can either ventilate a region or bring radionuclides into it.

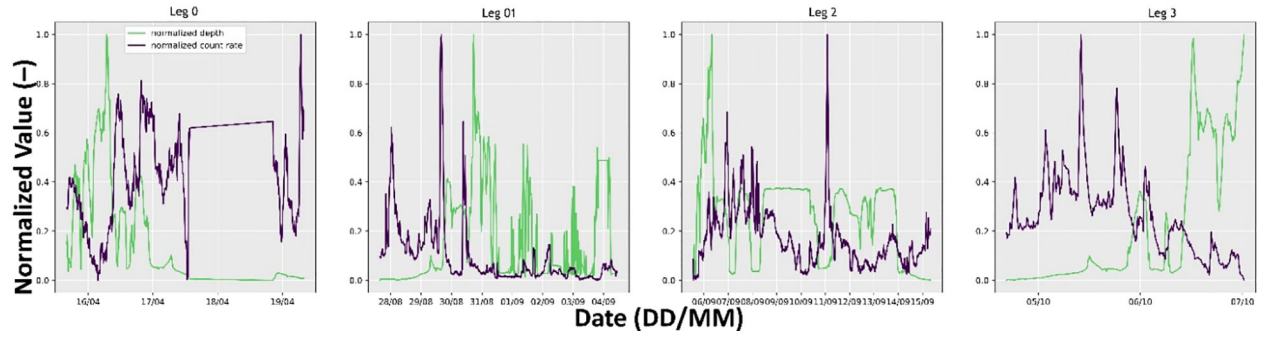

FIGURE 10
Time series of normalized depth and TC trends.

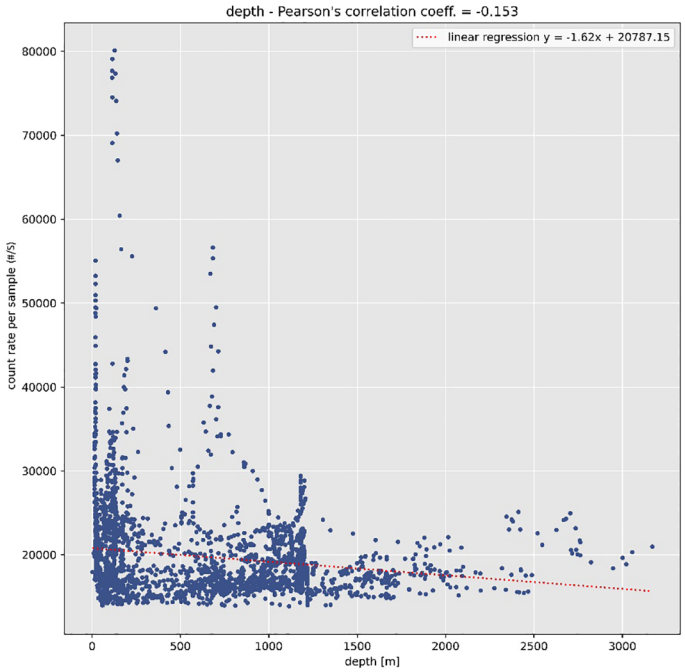

FIGURE 11
TC per sample vs depth correlation.

3.4.3 Temperature

While ambient temperature can influence radiation levels through environmental and instrumental mechanisms, the instrumental effect is corrected via calibration. The environmental mechanism involves temperature altering the marine boundary layer and the distribution of radionuclide carrying aerosols. This analysis therefore focuses solely on this atmospheric relationship. The correlation between temperature and the TC are seen in Figures 14, 15. Thus, there is weak reverse relation between temperature variation seems in the Figure 15.

3.4.4 Humidity

Atmospheric humidity is a crucial parameter in environmental radiation surveys due to its significant attenuating effect on gamma radiation. Variations in absolute humidity can substantially influence measured TCs, potentially creating false anomalies or masking real ones.

In this study, continuous humidity measurements were essential for applying accurate corrections to the raw radiation data. This correction protocol ensures that identified anomalies genuinely reflect terrestrial or aquatic sources, rather than

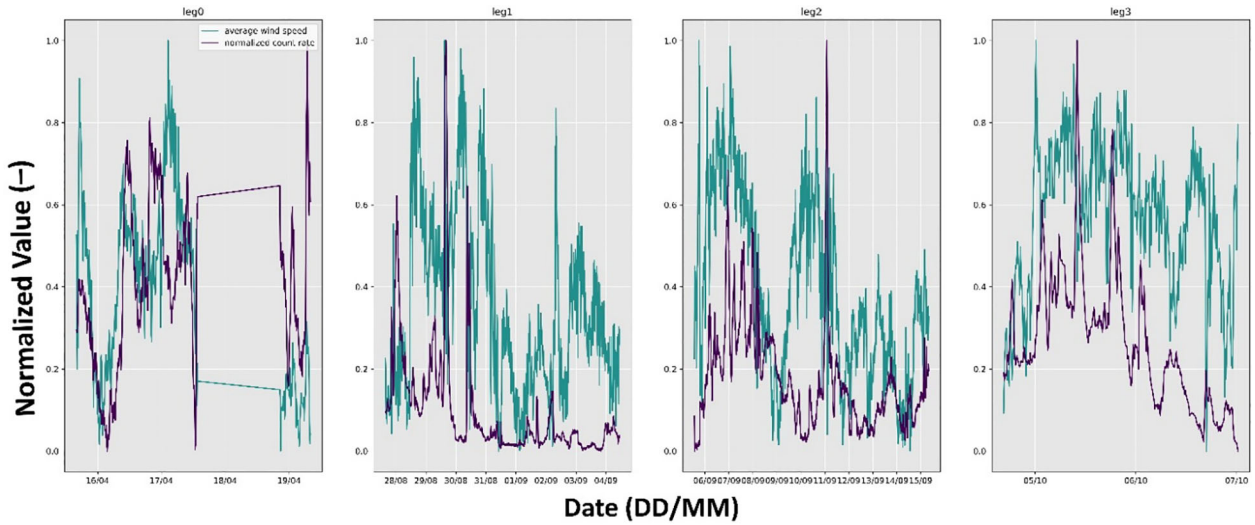

FIGURE 12
Time series of normalized wind and TC trends.

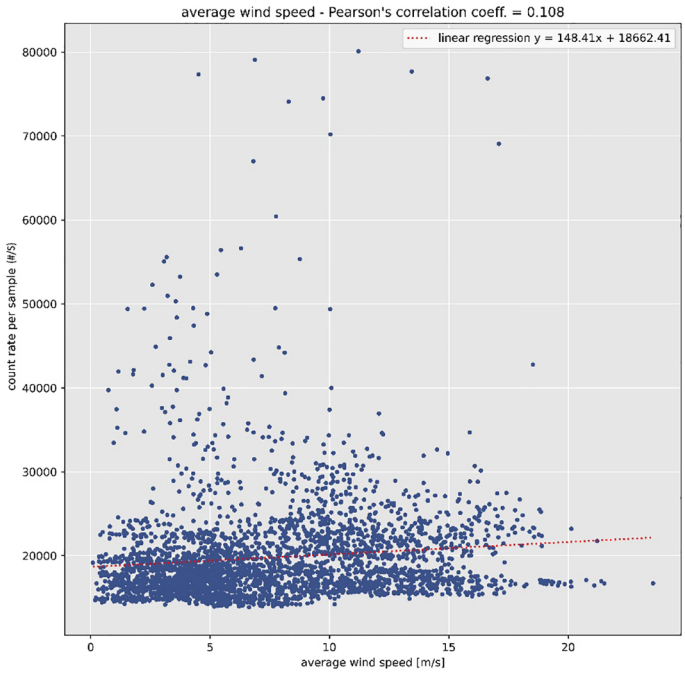

FIGURE 13
TC vs average wind speed correlation.

atmospheric artifacts, thereby validating the spatial patterns observed in the survey maps. As it is clear in the Figure 16 as well as theoretical expected there is a direct relation between humidity and also droplet size with measured TC. And also it is can be seen clearly in the Figure 17 trends this is not dominant phenomena which could described these anomalies regions, but clearly can affect specially measured peak values.

3.5 Comparison with previous studies, interpretation potential natural sources of the anomalies

To validate the research hypothesis, this section synthesizes and extends existing evidence concerning the existence and origin of the observed anomalies. This section systematically reviews the existence of anomalous regions, radionuclides, and sedimentary materials previously documented in scientific literature for areas analogous to those identified in this study. The content is organized into four regional subsections:

- Central Adriatic Sea
- Southern Adriatic Sea
- Strait of Otranto
- Aeolian Islands

This structured compilation will serve as a direct basis for interpreting the potential origins and processes behind the anomalous radiation signatures documented in this article's findings.

3.5.1 Northern and central Adriatic Sea

This region constitutes a critically important oceanic point, functioning as a hydrological convergence zone where the coastal

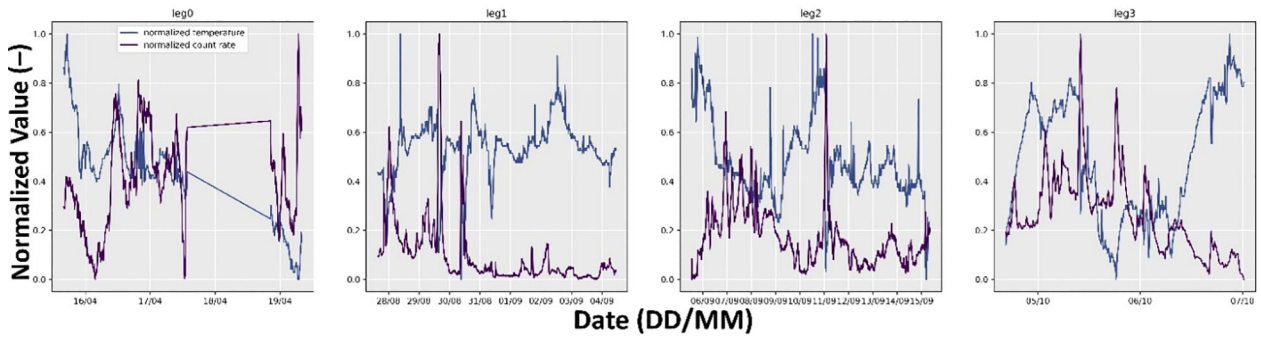

FIGURE 14
Time series of normalized temperature and TC trends.

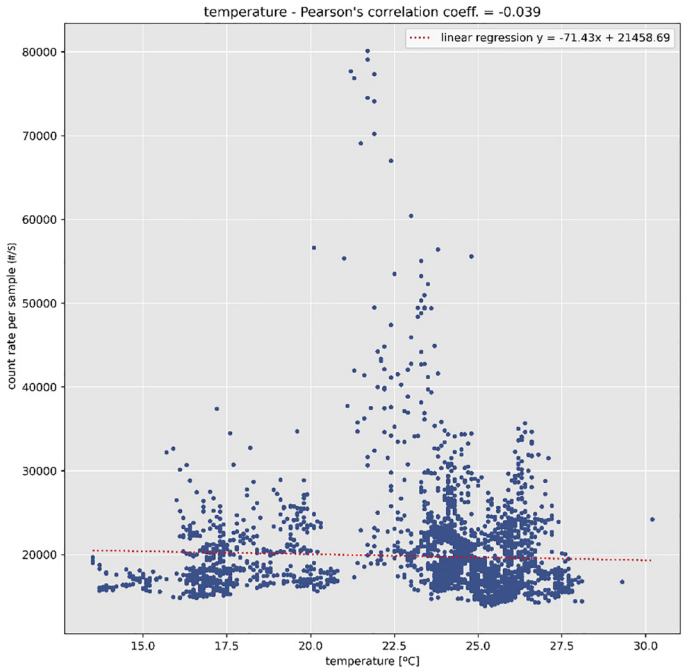

FIGURE 15
TC vs temperature correlation.

currents of Italy and Croatia meet and change direction which is shown in Figure 18 (Frascari et al., 1988). This circulation pattern establishes the area as a primary accumulation site for sediments. These sediments transport a significant load of pollutants, including industrial and urban discharges from northeastern Italian and southwestern Croatian rivers and coastal areas, combined with historical deposits of radionuclides from global fallout, such as the ^{90}Sr peak recorded in 1963 (Franic and Bauman, 1993). Another major process for the cross-shelf transport of particulate matter is the generation of North Adriatic Dense Water (NAdDW). During winter, cold, dense water formed on the shallow northern shelf cascades down the slope, acting as a conduit for sediments and adsorbed riverine contaminants, ultimately depositing them in the topographically confined Jabuka (Pomo) Pit and the Southern

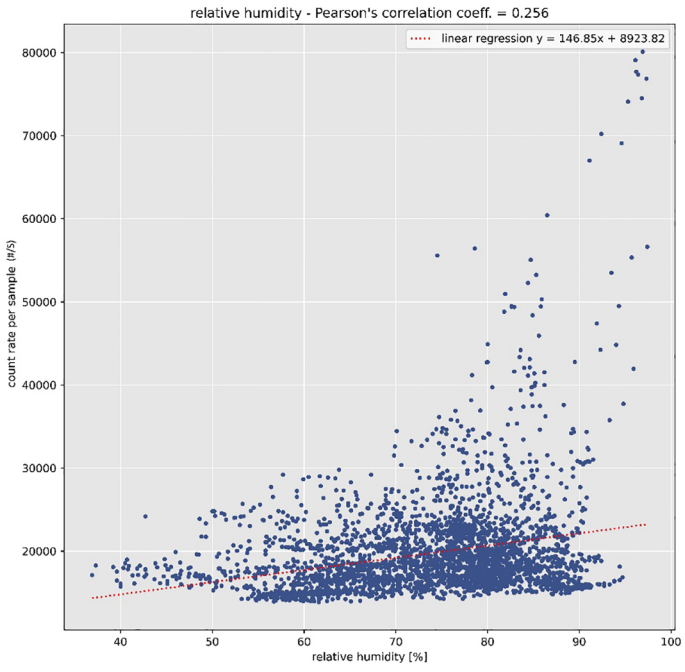

FIGURE 16
TC vs relative humidity correlation.

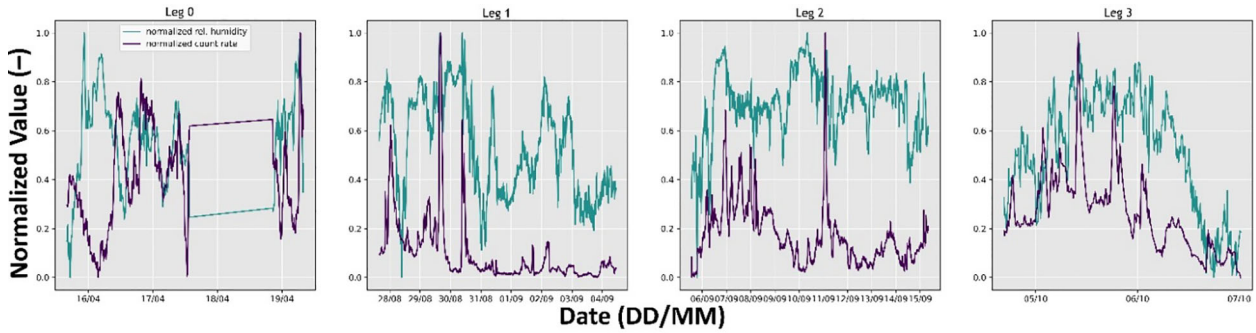

FIGURE 17
Time series of normalized humidity and TC trends.

Adriatic Pit which is visible in the blue line in the Figure 19 (Martellucci et al., 2025).

Consequently, the region is predisposed to concentrating both natural and anthropogenic radionuclides. This hypothesis is strongly supported by empirical data from this study, which identified this specific location as having the highest TC across all four research cruises.

3.5.2 Strait of Otranto

The SAP, the deepest basin of the Adriatic Sea (1,330 m), and the Otranto Strait, which connects the Adriatic to the Mediterranean Sea, are geographically significant regions. Analysis of sediment cores from these areas by Petrinec et al. revealed elevated activity concentrations of ^{226}Ra compared to other sampled locations in the Adriatic (Petrinec et al., 2013).

The MARIS (Marine Radioactivity Information System), maintained by the IAEA, is an open repository of standardized, quality-controlled measurements of radioactivity in seawater, sediments, and biota. For the Adriatic Sea (away from the coast), the MARIS database currently contains records for nine sampling points in the southern Adriatic and at the entrance to the Mediterranean Sea. Of these, only five originate from the same research project, using the same sampling instrument and depth, and measuring solely ^{137}Cs activity. Nevertheless, these data are worth mentioning due to the importance of this program. The data related to coordination and activity are located in the Table 3 and the sampling depth is zero meter, means water surface and samples type were sea water (Martin and Thomas, 1990).

There are two important results from this study (it is worth noting that these results are based on data from forty years ago and may differ over time with the introduction of new sources into the sea). First, in this study area, there is no significant jump in ^{137}Cs activity as a marker of anthropogenic material, neither in the MARIS data nor in the new dataset presented in this article. Second, the relationship between activity and count rate, as analyzed here, shows the same trend when comparing anomalous points with normal points.

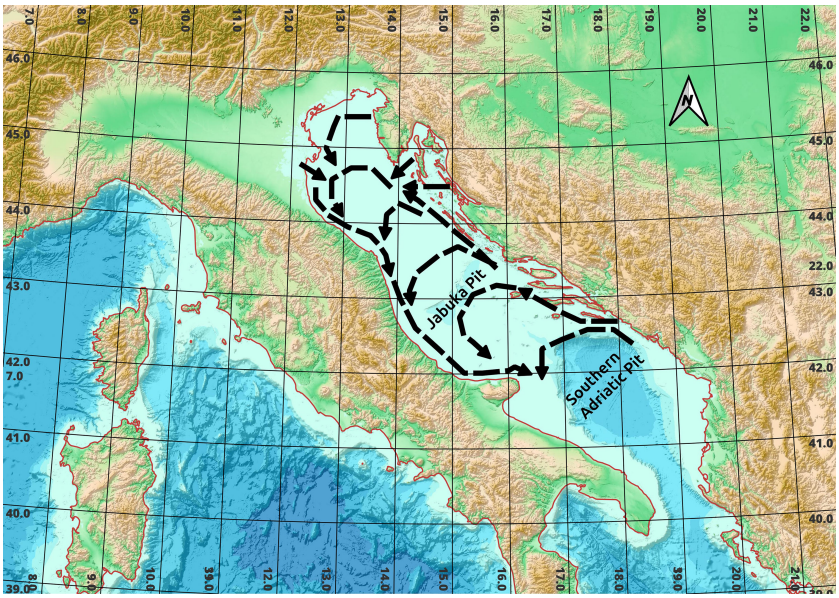

FIGURE 18
Circulation patterns in the Adriatic Sea (Frascari et al., 1988).

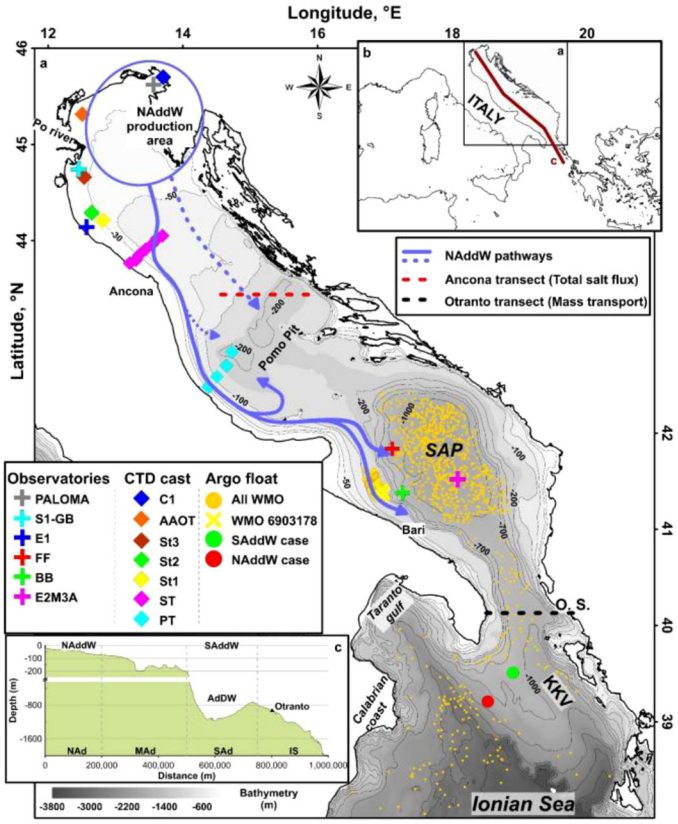

FIGURE 19
Adriatic and Ionian Sea pathways of the NAddW (blue line). Source: Reproduced from Martellucci et al. (2025), licensed under CC BY 4.0.

3.5.3 Aeolian Islands

Regarding the Aeolian Islands, it is clear that there is an active volcano and hydrothermal vent system (Spagnoli et al., 2024). However, higher radiological TCs were not observed in this area. Since the focus of this article is on the identified high TC anomalies, a more detailed interpretation of the Aeolian Islands region will not be pursued here and will be the subject of a future research cruise conducted on land and at sea.

3.5.4 Time base variation

As can explore from MARIS data ((IAEA), 1991; Aoyama and Hirose, 2004) and other marine gamma spectrometry studies, radionuclide concentrations in the marine environment can change rapidly due to dynamic processes like advection and dilution. This temporal variation is illustrated in Figure 20, which shows concentration changes over time at fixed coordinates. A similar pattern of temporal variation was observed in the present study. While the locations of the anomalous points were semi-consistent, the peak intensity along the transect from Trieste to Aeolian Islands showed significant change. A much sharper peak was recorded in August, which then dissipated, becoming less pronounced in September and substantially more diluted by October. Worth mentioning point is dynamic behavior of radionuclide concentration even in the water sample which is more stable than atmospheric record.

TABLE 3 Reported samples location.

Latitude	Longitude	^{137}Cs activity (Bq/m^3)
41.77 N	18.17 E	4.292
40.33 N	18.90 E	3.071
39.55 N	19.35 E	4.551
39.55 N	17.65 E	3.774
37.50 N	15.50 E	3.922

3.5.5 Recorded human based activities

To enhance the reliability of the analysis concerning anthropogenic influences, data from the European Marine Observation and Data Network (EMODnet) were consulted. The investigation revealed that the only notable human infrastructure near the most significant anomaly peaks are the planned offshore wind farms “NEREUS Offshore” and “Bluwind Manfredonia,” with considerable nominal powers of 2205 MW and 825 MW, respectively. The precise coordinates for these planned facilities are 41.800 N, 16.600 E and 41.890 N, 16.690 E near to most prominent peak region of this article which is near to 41.982 N, 16.503 E.

Although these wind farms have not been constructed, their planned locations align with the hotspot intersection of water circulation and wind patterns discussed in Section 4.5.1 and 4.5.2.

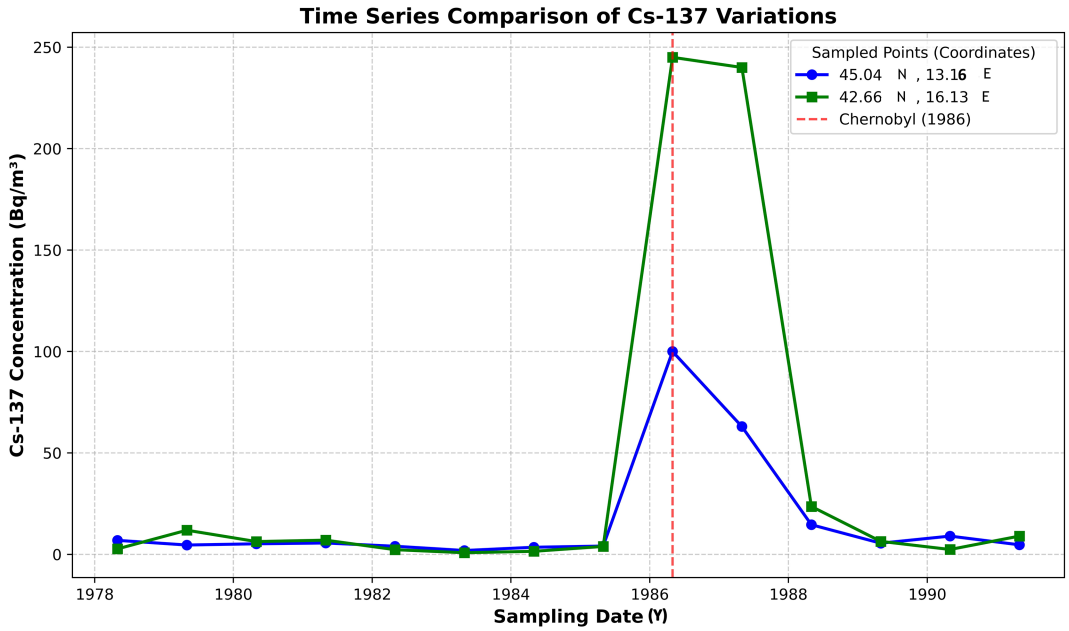

FIGURE 20
Time series comparison of ^{137}Cs variations.

This spatial correlation strengthens the hypothesis regarding the origin of the observed anomaly.

Furthermore, the hypothesis of a predominantly natural origin for these anomalies is supported by the distribution of nuclear facilities in Italy. As shown in Figure 21, Italy's two decommissioned nuclear power plants are located in the western part of the country, with no reported disposal of their waste materials in the eastern Adriatic. Therefore, even if the considered human facilities were to contribute materials to the North Adriatic Dense Water (NAdDW) or the broader Adriatic circulation, the potential for introducing significant amounts of anthropogenic radionuclides remains low. Consequently, the anomalies are more likely attributable to natural radiation from the Uranium, Thorium, and Potassium series and their decay chains.

3.5.6 Recorded geological based activities

To validate the hypothesis and identify the associated geological factors, a similar spatial analysis was conducted using data on

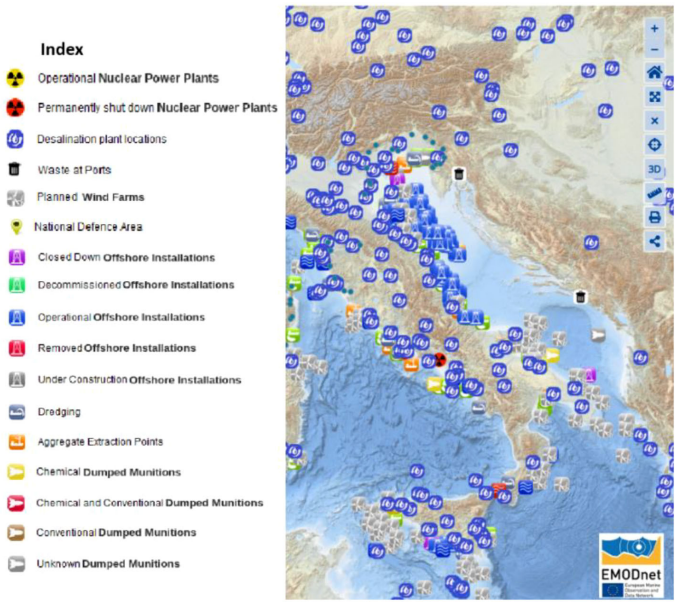

FIGURE 21
Recorded human based activities (Marine Renewable Energy - Wind Farms, 2024).

current locations, volcanoes, hydrothermal vents, and tectonic plate boundaries. As illustrated in Figure 22, the Adriatic Sea contains no reported major hydrothermal vents or submarine volcanoes. However, the presence of significant currents, as confirmed by EMODnet data, is evident. Notably, the strongest recorded current is located adjacent to the highest anomaly peak. This spatial correlation aligns the results and strengthens the hypothesis of a current-driven origin for the anomalies. Nevertheless, the possibility of undocumented hydrothermal vents cannot be entirely dismissed, leaving open the potential for a contributory role from such sources.

3.6 Interpretation

Three high TC anomaly regions were identified: one in the central Adriatic Sea, another in the southern Adriatic, and a third near the Strait of Otranto. The existence of these regions is supported by multiple marine surveys conducted under varying seasonal conditions, wind patterns, and sampling trajectories. Consequently, the persistence of these anomalies is considered robust.

The radiological anomalies detected in these regions have a multi-source provenance, integrating both natural and anthropogenic inputs. The natural component is primarily governed by the release of radionuclides from geological substrates and their transport by regional groundwater and fluid flow systems. The anthropogenic component, meanwhile, may include contributions from industrial effluents delivered by river systems and historic global fallout.

The spatial distribution of these anomalous peaks appears to be influenced by complex water circulation patterns and sediment dynamics. Secondary, temporal variations in the signal amplitude are modulated by dynamic environmental conditions, including temperature, wind fields, and hydrodynamic forcing.

It is critical to note that these findings do not preclude potential increases from anthropogenic sources. A comprehensive and extensive study on the spatial and historical variations of anthropogenic radionuclides will be detailed in a separate, dedicated article.

Regarding Radiological Protection aspect, following ICRP definitions, these anomalies contribute to the natural background dose. As such, they are not included in occupational dose limits for radiation protection. However, it is noteworthy that the elevated readings in these anomalous zones differ substantially from the local background levels, and this difference is considerable when viewed in the context of standard radiation protection criteria.

4 Conclusions

This study successfully identified and characterized three persistent offshore gamma radiation anomalies along the Trieste–Panarea transect through high-resolution, *in-situ* marine gamma-ray spectrometry. The analysis of over 4,000 recorded spectra acquired during four research cruises, covering more than 2,500 nautical miles, revealed three distinct and reproducible anomaly regions. These were located in the Central Adriatic (peak: 34,659 TC at ~43.09°N, 14.96°E), the Southern Adriatic (peak: 76,854 TC at ~41.98°N, 16.50°E), and the Strait of Otranto (peak: 32,415 TC at ~40.15°N, 18.60°E).

Spectral deconvolution of the recorded 1024-channel spectra conclusively determined the natural origin of these anomalies. The analysis identified prominent photopeaks from key "flag radionuclides": the Uranium series (^{214}Bi at 609 keV, ^{214}Pb at 352 keV), the Thorium series (^{208}Tl at 583 keV and 2615 keV), and the Potassium series (^{40}K at 1461 keV). Quantitatively, the signal-to-noise ratio (SNR) for these natural decay series exceeded 10 in

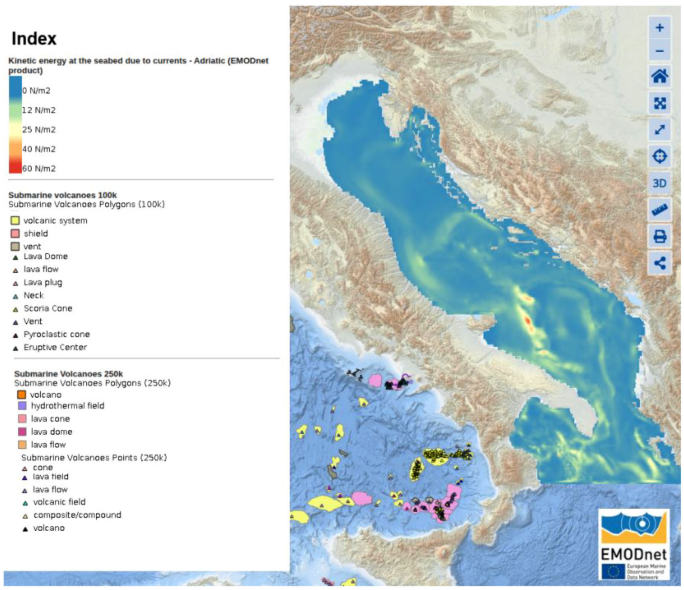

FIGURE 22
Recorded geological based activities (Marine Renewable Energy - Wind Farms, 2024).

the anomalous regions, while the anthropogenic indicator ^{137}Cs (662 keV) showed an SNR of <1, confirming its negligible contribution to the anomalous signal.

Critically, the data confirm that these anomalies are not artifacts of atmospheric conditions but are intrinsically linked to seabed sources and their redistribution by dominant water circulation currents. Weak statistical correlations between TC and atmospheric variables (wind, temperature, humidity; all $R^2 < 0.25$) rule out a dominant atmospheric driver. Instead, the persistent spatial correlation of the anomalies with specific oceanographic features the convergence zone of coastal currents in the Central Adriatic, the pathway of the North Adriatic Dense Water (NAdDW) cascading toward the Southern Adriatic Pit, and the dynamic interface at the Strait of Otranto provides the definitive explanation. These currents act as the primary mechanism for the hydrodynamic focusing and deposition of fine-grained, clay-rich sediments that are naturally enriched in potassium, uranium, and thorium. The anomalies thus mark the seafloor depocenters or sediment focusing zones created by this persistent circulation.

In summary, this research achieves three primary outcomes:

- ✓ It establishes the first high-resolution, continuous radiometric baseline for the Adriatic Sea, derived from synoptic, real-time *in-situ* measurements rather than discrete sampling.
- ✓ It conclusively attributes persistent offshore anomalies to natural sedimentary processes, where regional water circulation patterns are the fundamental control on the distribution of radiogenic seabed materials, as evidenced by spectral signatures dominated by the Uranium, Thorium, and Potassium decay series.
- ✓ It validates a robust methodological framework for real-time source discrimination, integrating full-spectrum gamma spectrometry with synchronized oceanographic data.

This work demonstrates that a real-time, integrated methodology synchronizing continuous spectral acquisition with oceanographic parameters enables a comprehensive interpretation of the marine radiometric environment, representing a foundational advancement for operational monitoring and research.

This integrated framework establishes the foundation for a future operational network, transforming research vessels into dynamic nodes for a real-time, radiological and oceanographic observing system.

Data availability statement

The raw data supporting the conclusions of this article will be made available by the authors, without undue reservation.

Author contributions

BS: Conceptualization, Data curation, Formal analysis, Investigation, Methodology, Software, Validation, Visualization, Writing – original draft, Writing – review & editing. MI: Formal analysis, Project administration, Software, Supervision, Writing – original draft, Writing – review & editing. AT: Data curation, Software, Writing – original draft, Writing – review & editing. FC: Funding acquisition, Resources, Supervision, Validation, Writing – original draft, Writing – review & editing.

Funding

The author(s) declared that financial support was not received for this work and/or its publication.

Acknowledgments

The author gratefully acknowledges the support of Radiation Solution Inc.

Conflict of interest

The author(s) declared that this work was conducted in the absence of any commercial or financial relationships that could be construed as a potential conflict of interest.

Generative AI statement

The author(s) declared that generative AI was not used in the creation of this manuscript.

Any alternative text (alt text) provided alongside figures in this article has been generated by Frontiers with the support of artificial intelligence and reasonable efforts have been made to ensure accuracy, including review by the authors wherever possible. If you identify any issues, please contact us.

Publisher's note

References

(IAEA) (1991). *I.A.E.A. Marine radioactivity information system (MARIS)*. Available online at: https://maris.iaea.org (Accessed November 1, 2025).

(IAEA), I.A.E.A., IAEA-TECDOC-1363 (2003). *Guidelines for radioelement mapping using gamma ray spectrometry data* (Vienna: International Atomic Energy Agency).

Aarkrog, A. (2003). Input of anthropogenic radionuclides into the World Ocean. *Deep Sea Res. Part II: Top Stud. Oceanogr* 50, 2597–2606. doi: 10.1016/S0967-0645(03)00137-1

Abdelhakim, A. (2025). Anomaly detection in gamma-ray radiation spectra using artificial neural network and ant colony optimization. *J. Environ. Radioact* 290, 107790. doi: 10.1016/j.jenvrad.2025.107790

Aoyama, M., and Hirose, K. (2004). Artificial radionuclides database in the Pacific Ocean: HAM database. *Sci. World J.* 4, 200–215. doi: 10.1100/tsw.2004.15

Barreca, G., Bruno, V., Cultrera, F., Mattia, M., Monaco, C., and Scarfì, L. (2014). New insights in the geodynamics of the Lipari–Vulcano area (Aeolian Archipelago, southern Italy) from geological, geodetic and seismological data. *J. Geodyn* 82, 150–167. doi: 10.1016/j.jog.2014.07.003

Bé, M. M., Chisté, V., Dulieu, C., Browne, E., Chechev, V., Kuzmenko, N., et al. (2004). Table of radionuclides 2.

Beamish, D., and Farr, G. (2013). Airborne geophysics: a novel approach to assist hydrogeological investigations at groundwater-dependent wetlands. *Q. J. Eng. Geol. Hydrogeol.* 46, 53–62. doi: 10.1144/qjegh2012-019

Bhat, M. (1992). "Evaluated nuclear structure data file (ENSDF)," in *Nuclear Data for Science and Technology: Proceedings of an International Conference, held at the Forschungszentrum Jülich, Fed. Rep. of Germany*, 13–17 May 1991 (Berlin, Heidelberg: Springer Berlin Heidelberg), 817–821.

Blake, G. H., and Topalović, D. (1996). *The maritime boundaries of the Adriatic Sea*, vol 1. (UK: International Boundaries Research Unit, University of Durham), 8.

Brown, D. A. (2018). ENDF/B-VIII. 0: the 8th major release of the nuclear reaction data library with CIELO-project cross sections, new standards and thermal scattering data. *Nucl. Data Sh* 148, 1–142. doi: 10.1016/j.nds.2018.02.001

Currie, L. A. (1968). Limits for qualitative detection and quantitative determination. *Appl. To Radiochem Anal Chem.* 40, 586–593. doi: 10.1021/ac60259a007

Dickson, B. L., and Scott, K. (1997). Interpretation of aerial gamma-ray surveys-adding the geochemical factors. *AGSO J. Aust. Geol Geophys* 17, 187–200.

Fisher, N. S., Beaugelin-Seiller, K., Hinton, T. G., Baumann, Z., Madigan, D. J., and Garnier-Laplace, J. (2013). Evaluation of radiation doses and associated risk from the Fukushima nuclear accident to marine biota and human consumers of seafood. *Proc. Natl. Acad. Sci.* 110, 10670–10675. doi: 10.1073/pnas.1221834110

Fitzgerald, S. A., Klump, J. V., Swarzenski, P. W., Mackenzie, R. A., and Richards, K. D. (2001). Beryllium-7 as a tracer of short-term sediment deposition and resuspension in the Fox River, Wisconsin. *Environ. Sci. Technol.* 35, 300–305. doi: 10.1021/es000951c

Franic, Z., and Bauman, A. (1993). Radioactive contamination of the adriatic sea by 90Sr and 137Cs. *Health Phys.* 64, 162–169. doi: 10.1097/00004032-199302000-00006

Frascari, F., Frignani, M., Guerzoni, S., and Ravaioli, M. (1988). Sediments and pollution in the northern adriatic sea a. *Ann. New York Acad. Sci.* 534, 1000–1020. doi: 10.1111/j.1749-6632.1988.tb30191.x

Gabbianelli, G., Gillot, P. Y., Lanzafame, G., Romagnoli, C., and Rossi, P. L. (1990). Tectonic and volcanic evolution of Panarea (Aeolian islands, Italy). *Mar. Geol* 92, 313–326. doi: 10.1016/0025-3227(90)90011-8

Giraldo, A. R., and Ramírez, J. S. (2023). Estimation of radioactive activity by gamma spectroscopy. *Rev. Investig Y Apl Nucl.* doi: 10.32685/2590-7468/invapnuclear.7.2023.667

Hirose, K., Igarashi, Y., and Aoyama, M. (2008). Analysis of the 50-year records of the atmospheric deposition of long-lived radionuclides in Japan. *Appl. Radiat. Isot* 66, 1675–1678. doi: 10.1016/j.apradiso.2007.09.019

Iurcev, M., Trebbi, A., Salmassian, B., Musco, M. E., and Coren, F. (2025). Gamma-ray spectrometry dataset along the route of the Research Vessel Laura Bassi during the Antarctic campaign. *Data Brief* 63, 112110. doi: 10.1016/j.dib.2025.112110

Iurcev, M., Pettenati, F., and Diviacco, P. (2021). Improved automated methods for near real-time mapping-application in the environmental domain. *Bull. Geophys Oceanogr* 62, 427–454. Available online at: https://hdl.handle.net/20.500.14083/19269.

Jones, D. (2001). Development and application of marine gamma-ray measurements: a review. *J. Environ. Radioact* 53, 313–333. doi: 10.1016/S0265-931X(00)00139-9

Knoll, G. F. (2010). *Radiation detection and measurement* (University of Michigan, Wiley: (John Wiley & Sons, Inc.)).

Krane, K. S. (1991). *Introductory nuclear physics* (United States of America: John Wiley & Sons).

Lal, D., and Peters, B. (1967). "Cosmic ray produced radioactivity on the Earth," in *Kosmische Strahlung II/cosmic rays II* (Berlin: Springer), 551–612.

Lee, M. S. (2017). Gamma-ray exposure rate monitoring by energy spectra of NaI (Tl) scintillation detectors. *J. Radiat. Prot. Res.* 42, 158–165. doi: 10.14407/jrpr.2017.42.3.158

Liu, C., Saull, P. R. B., Martin-Burtart, N., Hovgaard, J., Korpach, E., Tulk, C., Ungar, K., et al. (2022). Dose calibration of Health Canada's Fixed Point Surveillance system for environmental radiation monitoring in terms of air kerma and H*(10). *J. Environ. Radioact* 253, 107009. doi: 10.1016/j.jenvrad.2022.107009

Livingston, H. D., and Povinec, P. P. (2002). A millennium perspective on the contribution of global fallout radionuclides to ocean science. *Health Phys.* 82, 656–668. doi: 10.1097/00004032-200205000-00012

Marine Renewable Energy - Wind Farms (2024). *EMODnet human activities*. Available online at: https://emodnet.ec.europa.eu/en/human-activities (Accessed November 1, 2025).

Martellucci, R., Paladini de Mendoza, F., Menna, M., Pirro, A., Reale, M., Gačić, M., et al. (2025). A multiobservation analysis of the 2017 dense water formation events: Climate change, bottom density currents, and Adriatic-Ionian sea circulation (Mediterranean Sea). *J. Geophys Res: Ocean* 130, e2024JC022306. doi: 10.1029/2024JC022306

Martin, J., and Thomas, A. (1990). Origins, concentrations and distributions of artificial radionuclides discharged by the Rhône River to the Mediterranean Sea. *J. Environ. Radioact* 11, 105–139. doi: 10.1016/0265-931X(90)90056-2

Oyj, V. (2023). *User guide: vaisala weather transmitter WXT530 series*. Available online at: https://www.vaisala.com/en/products/weather-environmental-sensors/weather-transmitter-wxt530-series (Accessed November 1, 2025).

Pearson, K. (1896). "VII. Mathematical contributions to the theory of evolution.—III. Regression, heredity, and panmixia. Philosophical Transactions of the Royal Society of London," in *Series A, containing papers of a mathematical or physical character*, (London, England: Royal Society) vol. 1896, 253–318.

Periáñez, R. (2020). Models for predicting the transport of radionuclides in the Red Sea. *J. Environ. Radioact* 223, 106396. doi: 10.1016/j.jenvrad.2020.106396

Periáñez, R. (2019). Marine radionuclide transport modelling: Recent developments, problems and challenges. *Environ. Model. Softw* 122, 104523. doi: 10.1016/j.envsoft.2019.104523

Petrinec, B., Štrok, M., Franić, Z., Smodiš, B., and Pavičić-Hamer, D. (2013). Radionuclides in the Adriatic Sea and related dose-rate assessment for marine biota. *Radiat. Prot. Dosim* 154, 320–330. doi: 10.1093/rpd/ncs234

Povinec, P. P., Osvath, I., and Comanducci, J.-F. (2003). IAEA'97 expedition to the NW Pacific Ocean—results of oceanographic and radionuclide investigations of the water column. *Deep Sea Res. Part II: Top Stud. Oceanogr* 50, 2607–2637. doi: 10.1016/S1569-4860(07)11014-7

Povinec, P. P., Osvath, I., and Comanducci, J.-F. (2008). Underwater gamma-ray spectrometry. *Radioact Environ.* 11, 449–479. doi: 10.1016/S1569-4860(07)11014-7

Sanchez-Cabeza, J. A., and Ruiz-Fernández, A. C. (2012). 210Pb sediment radiochronology: an integrated formulation and classification of dating models. *Geochim Cosmochim Acta* 82, 183–200. doi: 10.1016/j.gca.2010.12.024

Spagnoli, F., Romeo, T., Andaloro, F., Canese, S., Esposito, V., Grassi, M., et al. (2024). Seeps and tectonic structure of the hydrothermal system of the panarea volcanic complex (Aeolian islands, tyrrhenian sea). *Geosciences* 14, 60. doi: 10.3390/geosciences14030060

Tyler, A. N. (1994). *Environmental influences on gamma ray spectrometry* (Glasgow Scotland: University of Glasgow).

Wilford, J., and Minty, B. (2006). The use of airborne gamma-ray imagery for mapping soils and understanding landscape processes. *Dev Soil Sci.* 31, 207–610. doi: 10.1016/S0166-2481(06)31016-1